NASA/CR-1999-209521

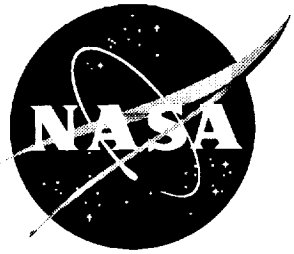

Computational Assessment of Aft-Body Closure for the HSR Reference H Configuration

W. Kelly Londenberg
ViGYAN, Inc., Hampton, Virginia

December 1999

The NASA STI Program Office . . . in Profile

Since its founding, NASA has been dedicated to the advancement of aeronautics and space science. The NASA Scientific and Technical Information (STI) Program Office plays a key part in helping NASA maintain this important role.

The NASA STI Program Office is operated by Langley Research Center, the lead center for NASA's scientific and technical information. The NASA STI Program Office provides access to the NASA STI Database, the largest collection of aeronautical and space science STI in the world. The Program Office is also NASA's institutional mechanism for disseminating the results of its research and development activities. These results are published by NASA in the NASA STI Report Series, which includes the following report types:

- TECHNICAL PUBLICATION. Reports of completed research or a major significant phase of research that present the results of NASA programs and include extensive data or theoretical analysis. Includes compilations of significant scientific and technical data and information deemed to be of continuing reference value. NASA counterpart of peer-reviewed formal professional papers, but having less stringent limitations on manuscript length and extent of graphic presentations.

- TECHNICAL MEMORANDUM. Scientific and technical findings that are preliminary or of specialized interest, e.g., quick release reports, working papers, and bibliographies that contain minimal annotation. Does not contain extensive analysis.

- CONTRACTOR REPORT. Scientific and technical findings by NASA-sponsored contractors and grantees.

- CONFERENCE PUBLICATION. Collected papers from scientific and technical conferences, symposia, seminars, or other meetings sponsored or co-sponsored by NASA.

- SPECIAL PUBLICATION. Scientific, technical, or historical information from NASA programs, projects, and missions, often concerned with subjects having substantial public interest.

- TECHNICAL TRANSLATION. English-language translations of foreign scientific and technical material pertinent to NASA's mission.

Specialized services that complement the STI Program Office's diverse offerings include creating custom thesauri, building customized databases, organizing and publishing research results . . . even providing videos.

For more information about the NASA STI Program Office, see the following:

- Access the NASA STI Program Home Page at ***http://www.sti.nasa.gov***

- Email your question via the Internet to help@sti.nasa.gov

- Fax your question to the NASA STI Help Desk at (301) 621-0134

- Telephone the NASA STI Help Desk at (301) 621-0390

- Write to:
  NASA STI Help Desk
  NASA Center for AeroSpace Information
  7121 Standard Drive
  Hanover, MD 21076-1320

NASA/CR-1999-209521

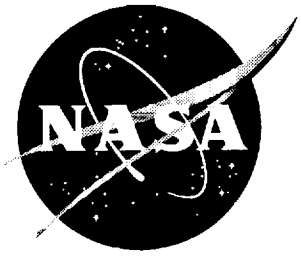

Computational Assessment of Aft-Body Closure for the HSR Reference H Configuration

W. Kelly Londenberg
ViGYAN, Inc., Hampton, Virginia

National Aeronautics and
Space Administration

Langley Research Center
Hampton, Virginia 23681-2199

Prepared for Langley Research Center
under Contract NAS1-19672

December 1999

Available from:

NASA Center for AeroSpace Information (CASI)
7121 Standard Drive
Hanover, MD 21076-1320
(301) 621-0390

National Technical Information Service (NTIS)
5285 Port Royal Road
Springfield, VA 22161-2171
(703) 605-6000

Computational Assessment of Aft-body Closure for the HSR Reference H Configuration

by
W.K. Londenberg
ViGYAN, Inc.
30 Research Drive
Hampton, VA 23666

Summary

A study has been conducted to determine how well the USM3D unstructured Euler solver can be utilized to predict the flow over the High Speed Research Reference H configuration with an ultimate goal of prediction of sting interference so after body closure effects may be evaluated. This study has shown that the code can be used to predict the interference effects of a lower mounted blade sting with a high degree of confidence. It has been shown that wing and fuselage pressures, both levels and trends, can be predicted well. Force and moment levels are not predicted well but experimental trends are predicted. Based upon this, predicted force and moment increments are assumed to be predicted accurately. Deflection of the horizontal tail was found to cause a non-linear increment from the non-deflected sting interference effects.

Introduction

The pursuit of interference free wind tunnel data has kept many an engineer gainfully employed since the wind tunnel was invented. Corrections have been developed to take into account the effect of wind tunnel walls and for blockage. The effect of the sting in configuration aerodynamics is minimized with the use of a straight, circular sting that intersects the aft end of the fuselage. This arrangement results in little interference, especially at lower angles-of-attack, since the sting can be treated as a streamtube. However, the aft body of the configuration being tested sometimes requires significant modification to accommodate this type of sting leading to the requirement for aft-body corrections. One method of wind tunnel model support that allows for the true after body to be modeled is a blade support that can intersect either the upper or lower fuselage surface forward of the empennage. This support structure, though, can no longer be treated as a streamtube and may cause significant interference on the configuration aerodynamics, especially at yaw angles and transonic speeds.

The purpose of this study is to first, validate the USM3D unstructured Euler solver for the prediction of flows about the High Speed Research Reference H configuration. A complete configuration will be

analyzed, including engine nacelles, horizontal tail and vertical tail. The second objective of this study is to numerically determine the affect of a lower, aft-mounted blade sting on the configuration aerodynamics. For this first study, sting effects will be determined only for the non-yawed configuration. These increments will be used to correct experimental data for sting interference so an empennage effect can be determined.

Symbols

b	span, inches
C_D	drag coefficient
C_L	lift coefficient
C_M	moment coefficient
C_p	pressure coefficient
F.S.	fuselage station, inches
M	freestream Mach number
Rn	Reynolds number, based on mean aerodynamic chord
y	span-wise dimension, inches
α	angle of attack
ΔC_D	drag coefficient increment
ΔC_L	lift coefficient increment
ΔC_M	moment coefficient increment
ΔC_p	pressure coefficient increment
δ	deflection angle, degrees

Subscripts:

HT	horizontal tail
LE	leading-edge
TE	trailing-edge

Method Description

The computational method utilized for this study was the USM3D Euler solver developed by Frink, Parikh and Pirzadeh[1]. This code utilizes an upwind numerical scheme to solve the time-dependent, three dimensional Euler equations on an unstructured tetrahedral mesh. A cell-centered finite-volume formulation is employed with both Roe's flux-difference splitting and Van Leer's flux-vector splitting available for spatial differencing.[2] Solutions are advanced in time to steady-state conditions by means of an implicit Gauss-Seidel algorithm described in reference 2. A first order interpolation scheme as well as a higher order scheme are also available.

Generation of the unstructured meshes used in this study was accomplished via the GridTool[3] and the VGRID[4,5 and 6] software. These codes develope the computational grid using the advancing front technique. Details of each code can be found in the respective references.

Grid Generation

Semi-span unstructured grids were constructed for this study about the High Speed Research (HSR) Reference H configuration for various leading and trailing edge flap configurations as listed in table 1. Grids were developed for the configuration with a lower mounted blade sting, a configuration with a circular aft body and circular sting, as well as for the configuration with no wind tunnel support structure modeled (referred to as the "free air" configuration). In all cases the horizontal and vertical tail as well as the engine nacelles and diverters were modeled. Computational meshes were also developed about the configuration with a -5° horizontal tail deflection. No grids were constructed for a rudder deflection. A view of a typical surface mesh is shown in figure 1. A detailed view of the wing lower surface showing the 30° leading-edge and 20° trailing-edge flap deflection as well as the nacelles and diverters is presented in figure 2.

Results

Code Validation

Solutions have been obtained for the HSR Reference H configuration at the conditions listed in table 1. The locations of experimental wing and fuselage surface pressure coefficients are shown in figures 3 and 4. Pressure coefficients obtained from the USM3D Euler calculations are compared with unpublished experimental data in figures 5 - 31. (The experimental data was obtained in the National Transonic Facility (NTF) at NASA Langley Research Center.) All solutions were obtained utilizing the higher order interpolation scheme and flux difference splitting with the exception of the M=0.95, α=8° solutions. These solutions (with and without the blade sting modeled) were only obtainable using first order interpolation and flux vector splitting.

The wing surface pressure coefficient plots exhibited in figures 5 - 9 show comparison of experimental data and computational results for an angle-of-attack variation at 0.95 Mach number. The theory predicts the experimental data well for all but the higher angle-of-attack cases. Here, as expected, the inviscid theory does not predict the apparent leading-edge vortex, a viscous phenomenon, evident in the experimental data (figures 8 and 9, Fuselage Stations 46.5 and 49.55). The code shows equally as good agreement with experiment for a deflected horizontal tail geometry (figures 10 and 11). Undeflected horizontal tail experimental data is used for comparison since deflection of the horizontal tail should not

significantly affect the wing surface pressures. At subsonic conditions with large leading and trailing edge flap deflections the theoretical method predicts the experimental results reasonably well (figure 12).

The plots presented in figures 13 - 17 show good comparisons of predicted fuselage surface pressure coefficients with experimental levels for a circumferential distribution of pressure taps at Fuselage Station 65.306 as angle-of-attack is increased for 0.95 Mach number. Note that the computational method is predicting the break in the experimental data in figures 13 - 17 between azimuth angles of 105° and 150°. Good comparisons are also obtained for a horizontal tail deflection at transonic conditions (figures 18 and 19). (The experimental data used in these comparisons was obtained for a geometry with deflected horizontal tail.) Figure 20 shows that a large trailing-edge deflection at subsonic speeds does not lower the quality of the comparisons. In fact, the comparisons at this condition is even more favorable than the transonic comparisons with undeflected inboard flaps.

Surface pressure comparisons along a line 45° below the horizontal extending from F.S. 65.306 to F.S. 81.04 for angle-of-attack varying from 0° to 8° is shown in figures 21 to 25 at 0.95 Mach number. In general, the theory agrees well with experiment, predicting the trend of the data well. The effect of a deflected horizontal tail is also predicted (figures 26 and 27). There is excellent agreement of computed results with experimental data for the subsonic case with large flap deflections (figure 28). These plots show there is a significant effect of blade sting interference on the aft-fuselage surface pressures and that when the geometry analyzed is consistent with the wind tunnel model, much better agreement with experimental levels are obtained.

Comparisons of predicted lift, drag and pitching moment with unpublished experimental values are shown in figures 29 - 30. The experimental data has not been corrected for aeroelastic effects. The Euler method predicts higher lift coefficient levels and more negative pitching moments than observed in the experiment (figure 29). These differences are consistent with those resulting from small aeroelastic effects. However, the trends of both lift and pitching moment with angle-of-attack are captured in the computed results. An increase in drag is also predicted at each angle-of-attack over the experimental level as would be expected with an over prediction of lift. (Note that the equivalent flat plate skin friction drag coefficient for eighty million Reynolds number has been added to the predicted drag coefficients.) However, when drag coefficient is plotted against lift coefficient (figure 30), the comparison of predicted values with experiment improves significantly.

These comparisons presented in figures 5 - 30 shows that the USM3D Euler method, while not predicting absolute levels, predicts overall trends in the experimental data well. This suggests that this code can be utilized to predict force and moment increments due to the blade sting support structure.

Sting Interference Predictions

Fuselage incremental surface pressure coefficients resulting from the interference of the blade sting in the computational analysis at 0.95 Mach number are presented in figure 31 (streamwise) and figure 32 (circumferential) with force and moment increments shown in figure 33. For both the calculations with and without the sting, the flaps on only the outboard portion of the wing were deflected -- 10° down along the leading-edge and 3° down along the trailing-edge. The predicted increments are calculated by subtracting the levels obtained from the analysis of the configuration without any sting support structure modeled from the levels resulting from analysis of the configuration with the blade sting modeled.

Pressure increments presented in figures 31 and 32 reveal that the effect of the blade sting support structure on the aft fuselage lower surface pressures is moderately independent of angle-of-attack. The effect of the fuselage surface pressure coefficients is shown to diffuse fairly quickly aft of the sting (see figures 4 and 31). Interference of the sting on the predicted total force and moment coefficients results in an increase in lift over the free air configuration, an increment that decreases with increasing angle-of-attack (figure 33, table 3). The presence of the blade sting also causes an increase in drag at all angles-of-attack but 0° (figure 33) where there is a slight drag decrement. The effect of the sting on predicted drag coefficient is shown to increase with increasing angle-of-attack. A stabilizing pitching moment increment is predicted as a result of sting interference (figure 33). It should be noted in the charts presented in figures 31 and 33 that the data plotted for 8° angle-of-attack were obtained from solutions utilizing flux vector splitting and first order interpolations as opposed to flux difference splitting and higher order interpolation. This would tend to introduce more diffusion into the numerical scheme which could result in the sharp decrease in lift coefficient as is evident in figure 33.

A more detailed analysis of the pressure coefficient increment, at 0.95 Mach number and α=4°, resulting from the blade sting is presented in figures 34 - 36. For this analysis, only the outboard wing flaps were deflected -- 10° down along the leading-edge and 3° down along the trailing-edge. The increments were calculated by interpolating the solution for the free air configuration onto the unstructured mesh developed about the configuration with the blade sting modeled. Increments are computed by subtracting the interpolated free air levels from the levels of the configuration with the blade sting. For clarity, contour lines for ΔC_p=0 are not plotted. The pressure coefficient map presented in figures 34 and 35 shows that the sting affects the fuselage lower surface pressures as expected -- a relative compression at the leading-edge of the sting, a relative expansion around the sting and a relative compression at the trailing-edge of the sting. (The sting has an airfoil cross section (see figure 4).) Notice also the tight clustering of contour lines along the leading-edge of the horizontal tail. An unexpected result of sting interference is the compression that is seen between the nacelles (figures 35 and 36). (The pentagonal

and hexagonal contour patterns are not real but are due to numeric anomalies in the interpolation algorithm.) The data presented in figures 31 and 32 suggest that similar surface pressure increment trends should be expected for the additional Angles-of-attack analyzed.

Examination of the previous charts yields some explanation of the behavior of the force and moment increment curves of figure 33. The sting interference causes more positive pressures over the lower surface of the aft portion of the wing as is shown in figure 35. This would result in increased lift as well as more nose-down (negative) pitching moment since the moment reference center is forward of this portion of the wing (figure 3). Since the prediction method solves the Euler equations and thus is inviscid, any drag predicted is purely a function of pressure. Therefore, an increase in lift due to the sting would lead to an expectation that drag would also increase. This is generally the case with the exception of the 0° angle-of-attack solution. Here, where the sting causes the largest lift increment, a drag decrement is predicted (figure 33). The data presented in figures 29 and 30 reveals that the minimum drag in the experimental data as well as in the computed drag for the free air configuration occurs near 1° angle-of-attack. A small increase in lift from the 0° angle-of-attack value moves the data point to the right along the drag polar towards the minimum drag point and therefore to a lower drag level.

The change in angle-of-attack that results from the presence of the blade sting is shown by the data plotted in figure 37. This chart shows the amount that the free air configuration angle-of-attack would need to be increased so that the lower surface pressures at the 50% semi-span location would match those computed for the configuration with the blade sting modeled. (Any change in lower surface pressure coefficient would be an indication of a change in angle-of-attack.) It is evident that the effective angle-of-attack increase is indeed less than a degree at 0° angle-of-attack. Effective up-wash induced by the blade sting is also shown to increase with angle-of-attack.

The effect of the blade sting on configuration forces and moment when the horizontal tail is deflected -5° (leading-edge down) is also presented in figure 33. This figure indicates that deflection of the horizontal tail causes a non-linear change in the blade interference from the δ_{HT}=0° configuration.

The surface pressure increments for 0.30 Mach number and six degrees angle-of-attack are presented in figures 38-41. In this analysis the inboard and outboard leading-edge flaps were deflected 30° and the inboard and outboard trailing-edge flaps were deflected 20°. The increments are again calculated as the difference between the sting on results and the sting off results. For clarity, contour lines for ΔC_p=0 are not plotted. These charts show that the sting had little effect on the lower wing surface pressures. As a result of sting/trailing-edge flap deflection interference, a relative compression, a relative expansion and another relative compression, all near the leading-edge of the fuselage-sting junction, is evident in figures 40 and 41. Notice the smaller effect of the sting on the aft fuselage at the subsonic conditions as compared to the

transonic analysis (compare figure 38 with figure 34). The relative compression between the nacelles evident in figure 35 for the transonic conditions is not predicted in the subsonic analysis (figure 39).

Aft Body Closure Corrections

The contribution of the afterbody on total force and moment coefficients is shown in figure 42. The computational increments were determined by integration of the predicted inviscid pressures of the free air configuration over only the aft fuselage and tail surfaces. Corresponding equivalent flat plate skin friction drag coefficients are also presented. The experimental increments were obtained by differencing the force and moments of the complete configuration and a truncated afterbody configuration. The experimental data has been corrected for blade interference utilizing the predicted increments shown in figure 33 and tabulated in table 3. Also presented in figure 42 is an increment showing the tolerance level for each force and moment increment plot. In general, there is good agreement between the Euler results and the corrected experimental data. However, there is some significant differences, the nature of which is not fully understood. The differences are partially due to the lack of viscous effects in the computational method. The uncertainty in the experimentally data as well as variability in the seal around the sting/ fuselage intersection are also possible causes of these differences.

Conclusions and Recommendations

From this study, it can be concluded that the USM3D unstructured Euler solver can be used to predict the aerodynamic trends for the HSR Reference H configuration. Even though numerical difficulties were encountered in the solutions at 8° angle-of-attack, the code can predict both the levels and trends of the experimental wing and fuselage surface pressures across the angle-of-attack range analyzed. Since the purpose of this study is to be able to predict sting increments, the inability to predict absolute force and moment levels is not too significant since the experimental trends are computed well. It can also be concluded from the figures presented that the blade sting causes an increase loading over the aft portion of the lower surface of the wing. This results in an increase in lift and drag and a more nose down pitching moment.

For future work, it is recommended that an unstructured grid about a full span configuration be developed so that predictions of sting interference at yaw angles may be made. This will necessitate that the geometry modeled include less detail than that used in the present study since this semi-span grid utilized nearly 200 megawords of computer memory to run. The only other recourse would be for the USM3D code to be modified to utilize less memory. It is also recommended that Navier-Stokes solutions utilizing the semi-span grid be obtained as soon as the viscous version of USM3D and the corresponding grid generation software is available.

Acknowledgments

This research was sponsored, in part, by the national Aeronautics and Space Administration under Contract NAS1-19672. Computations were partially performed on the National Aerodynamic Simulation Facility Cray C-90 and this support is gratefully acknowledged. The assistance of Dr. Shahyar Pirzadeh, Dr. Paresh Parikh, Dr. Neal Frink, and Javier Garriz in the use of the grid generation codes and the flow solver is appreciated. The unpublished NTF wind tunnel data was provided by Dr. Richard Wahls and Lewis Owens.

References

1)Frink, N.T., Parikh, P., and Pirzadeh, S.: "A Fast Upwind Solver for the Euler Equations on Three-Dimensional Unstructured Meshes," AIAA-91-0102, January 7-10, 1991.

2)Frink, N.T.: "Recent Progress Toward a Three-Dimensional Unstructured Navier-Stokes Flow Solver," AIAA-94-0061, January 10-13, 1994.

3)Samareh-Abolhassani, Jamshid, *GridTool User's Manual, Version 2.6,* Computer Sciences Corporation, Hampton, Va., April 1994.

4)Parikh, P., Pirzadeh, S., and Löhner, R.: "A Package for 3-D Unstructured Grid Generation, Finite-Element Flow Solutions, and Flow-Field Visualization," NASA CR-182090, September 1990.

5)Pirzadeh, S., "Structured Background Grids for Generation of Unstructured Girds by Advancing Front Method," *AIAA Journal,* Vol. 31, No. 2, February 1993, pp. 257-265.

6)Pirzadeh, S., "Recent Progress in Unstructured Grid Generation," AIAA Paper 92-0445, January 1992.

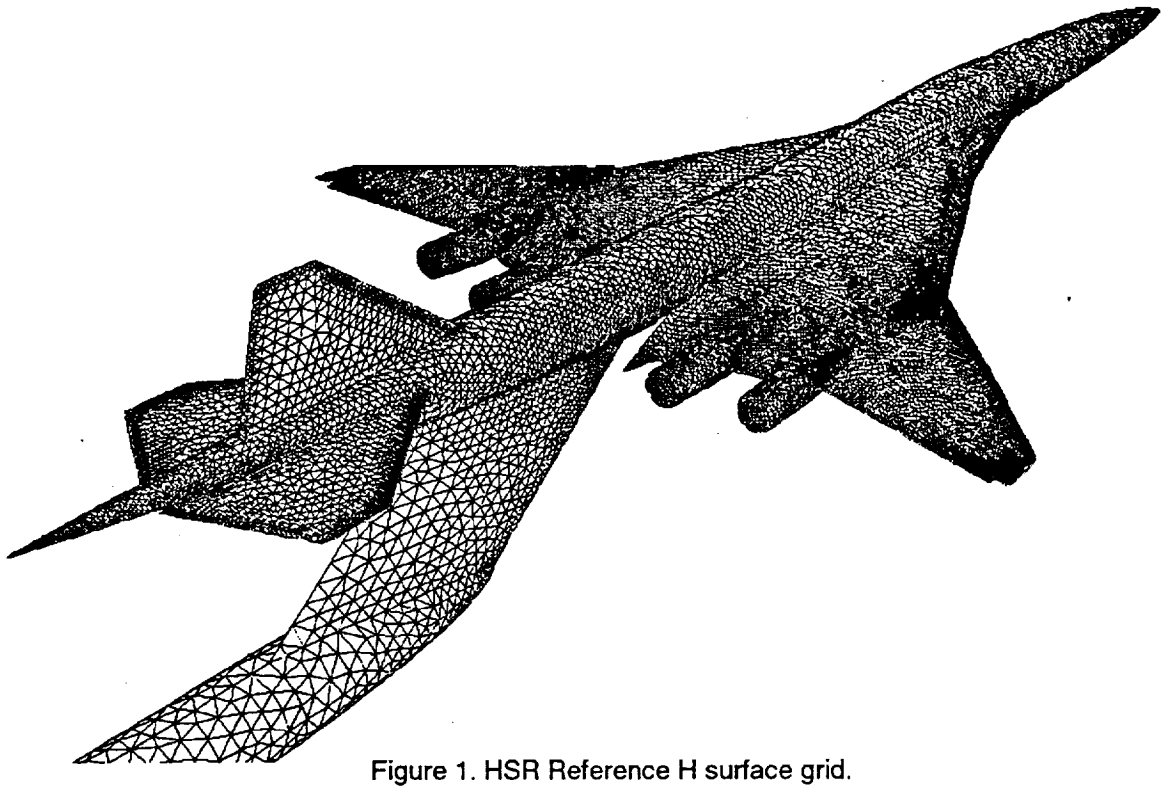

Figure 1. HSR Reference H surface grid.

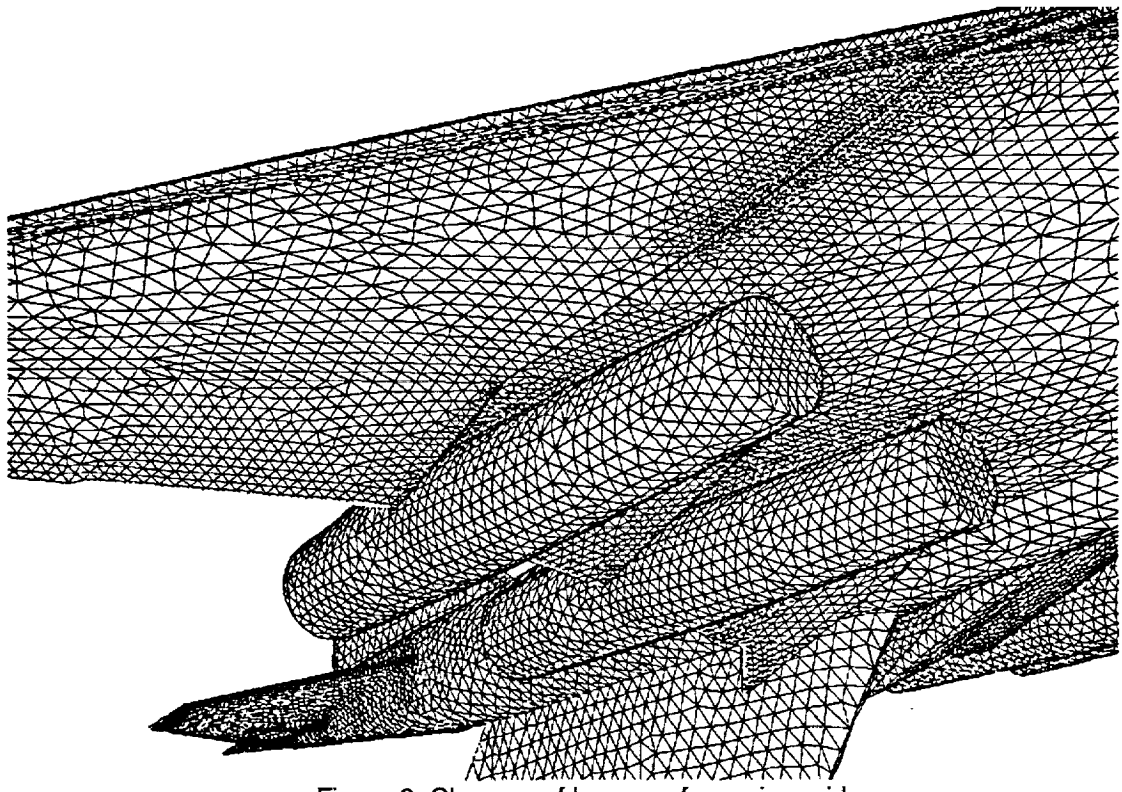

Figure 2. Close-up of lower surface wing grid.

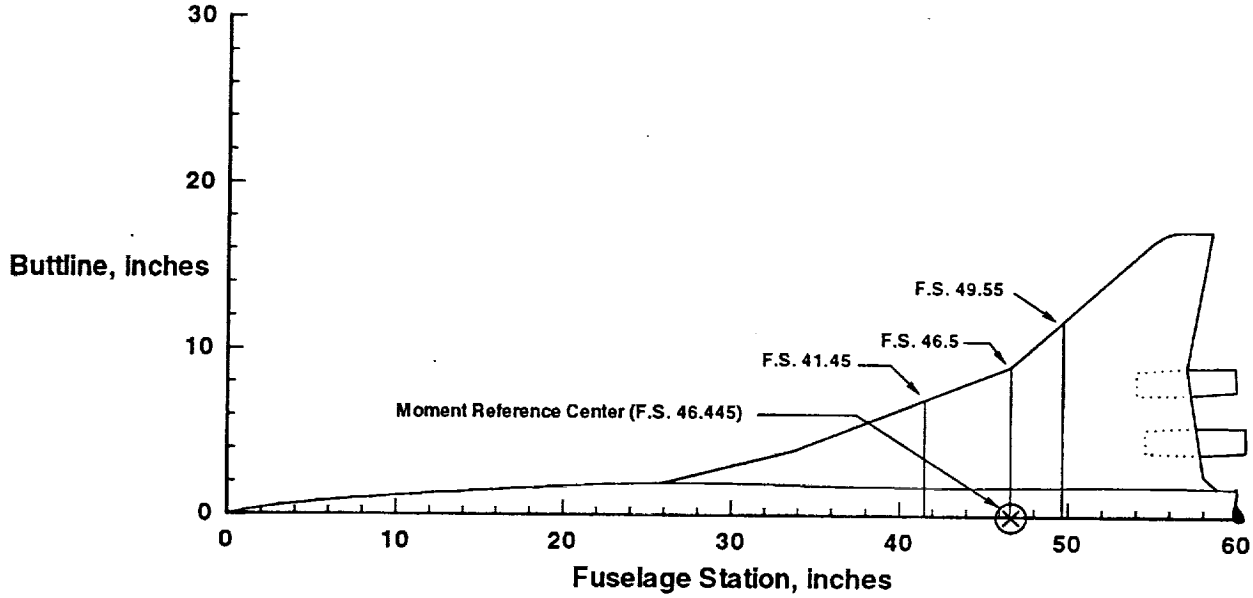

Figure 3. Planform view showing location of experimental wing pressure port rows.

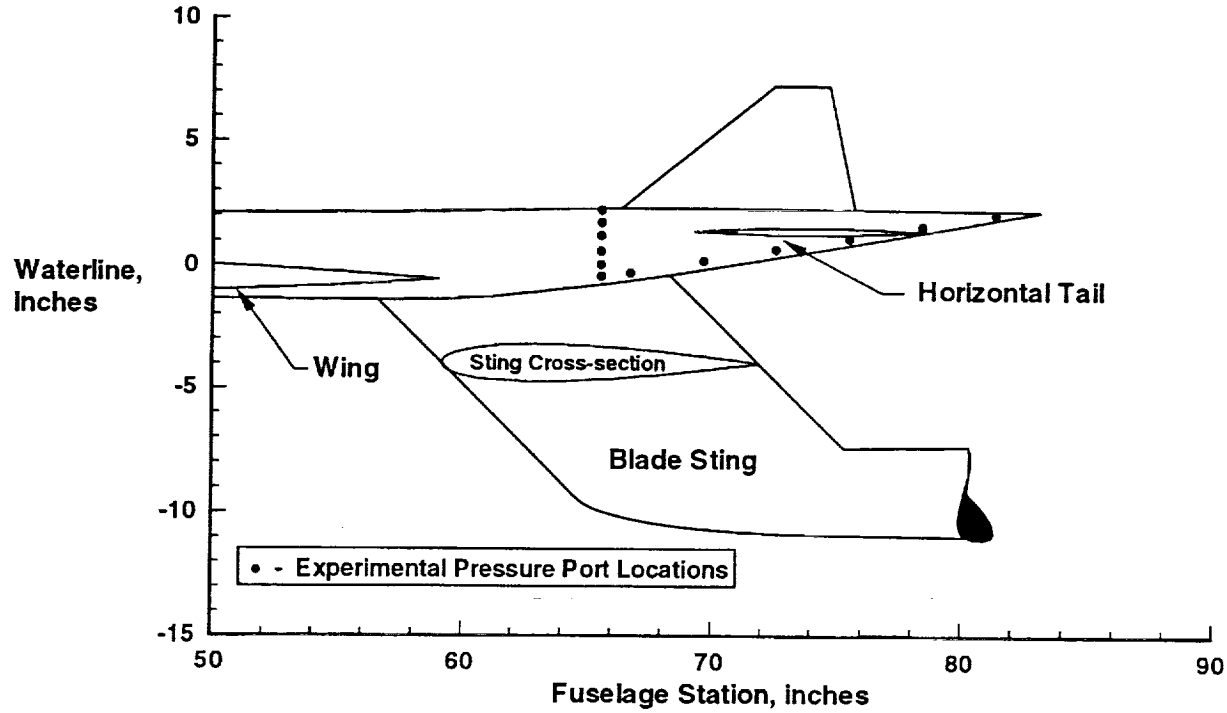

Figure 4. View of the HSR Reference H aft body showing the empennage and blade sting locations.

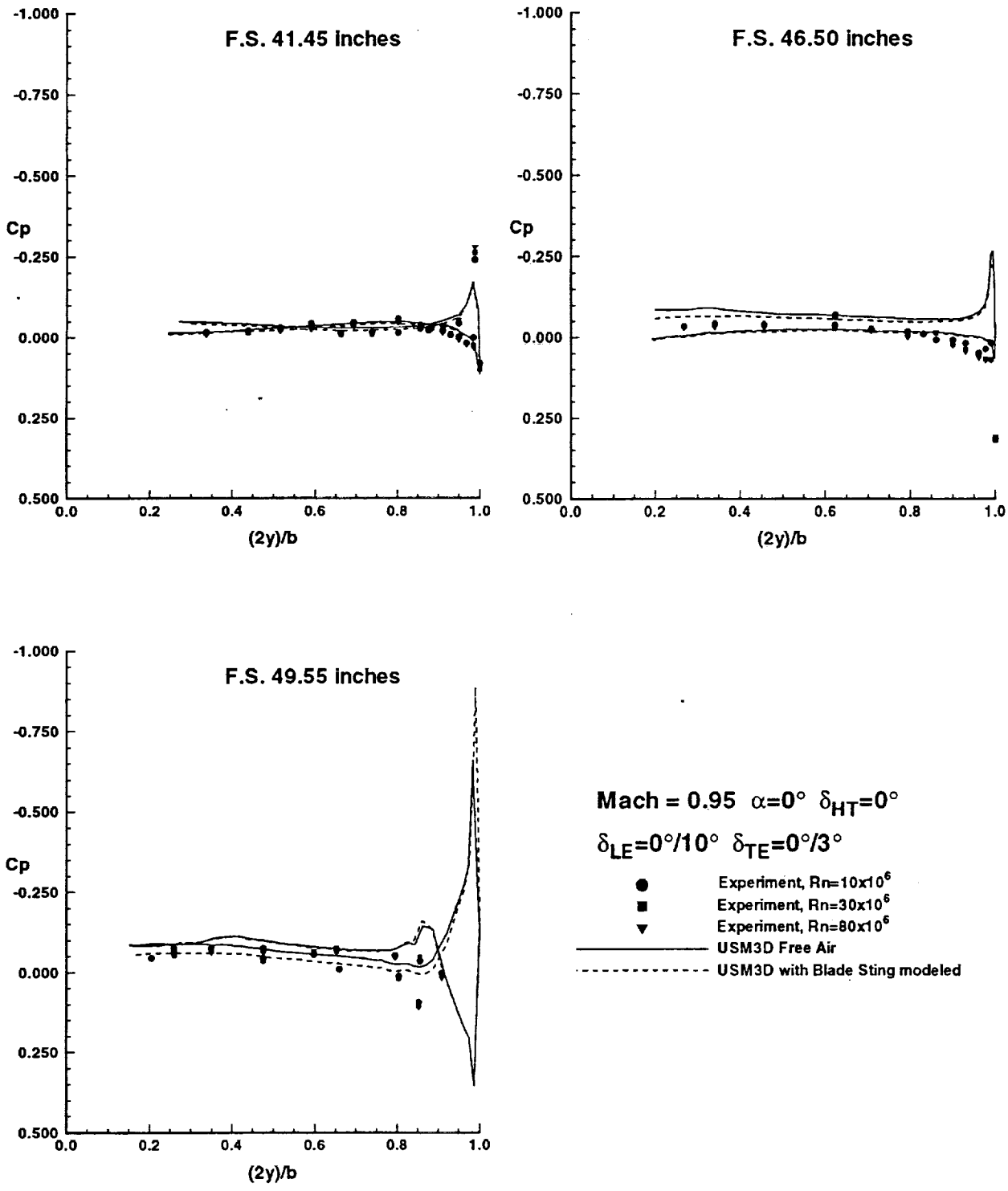

Figure 5. Comparison of predicted and experimental wing surface pressure coefficients; M=0.95, $\alpha=0^{\circ}$, $\delta_{HT}=0^{\circ}$, $\delta_{LE}=0^{\circ}/10^{\circ}$, $\delta_{TE}=0^{\circ}/3^{\circ}$.

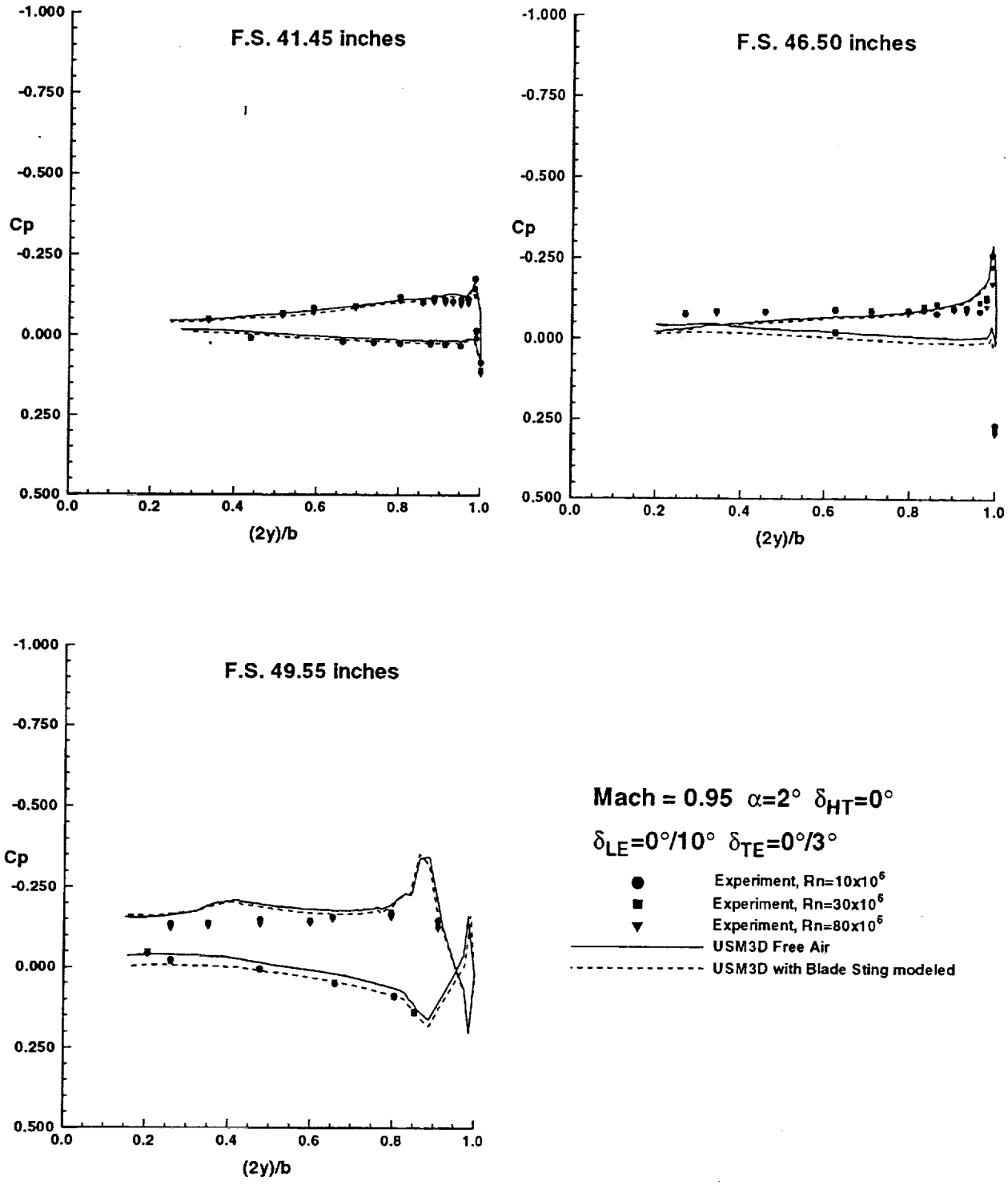

Figure 6. Comparison of predicted and experimental wing surface pressure coefficients; M=0.95, α=2°, δ_{HT}=0°, δ_{LE}=0°/10°, δ_{TE}=0°/3°.

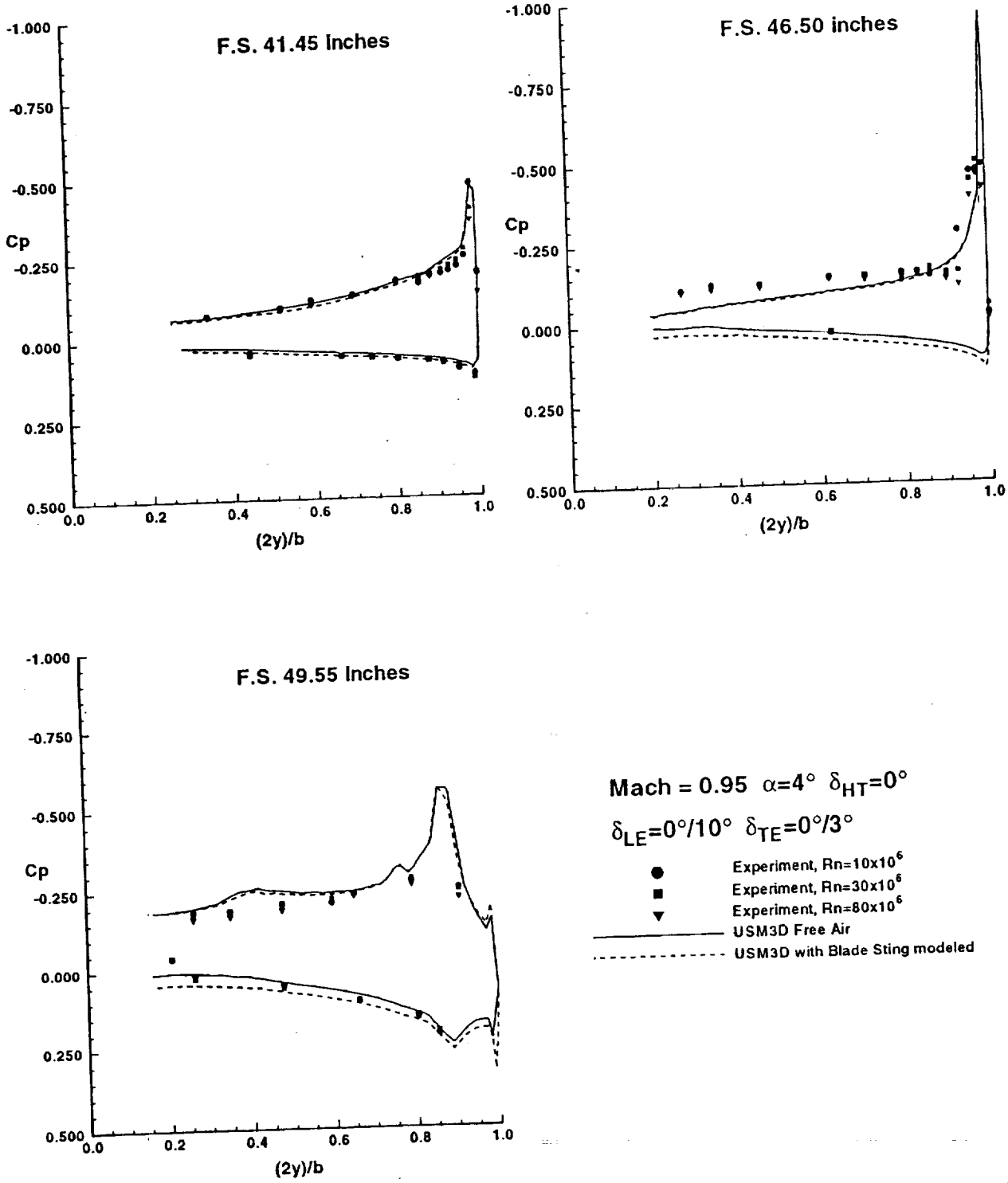

Figure 7. Comparison of predicted and experimental wing surface pressure coefficients; M=0.95, $\alpha=4^{\circ}$, $\delta_{HT}=0^{\circ}$, $\delta_{LE}=0^{\circ}/10^{\circ}$, $\delta_{TE}=0^{\circ}/3^{\circ}$.

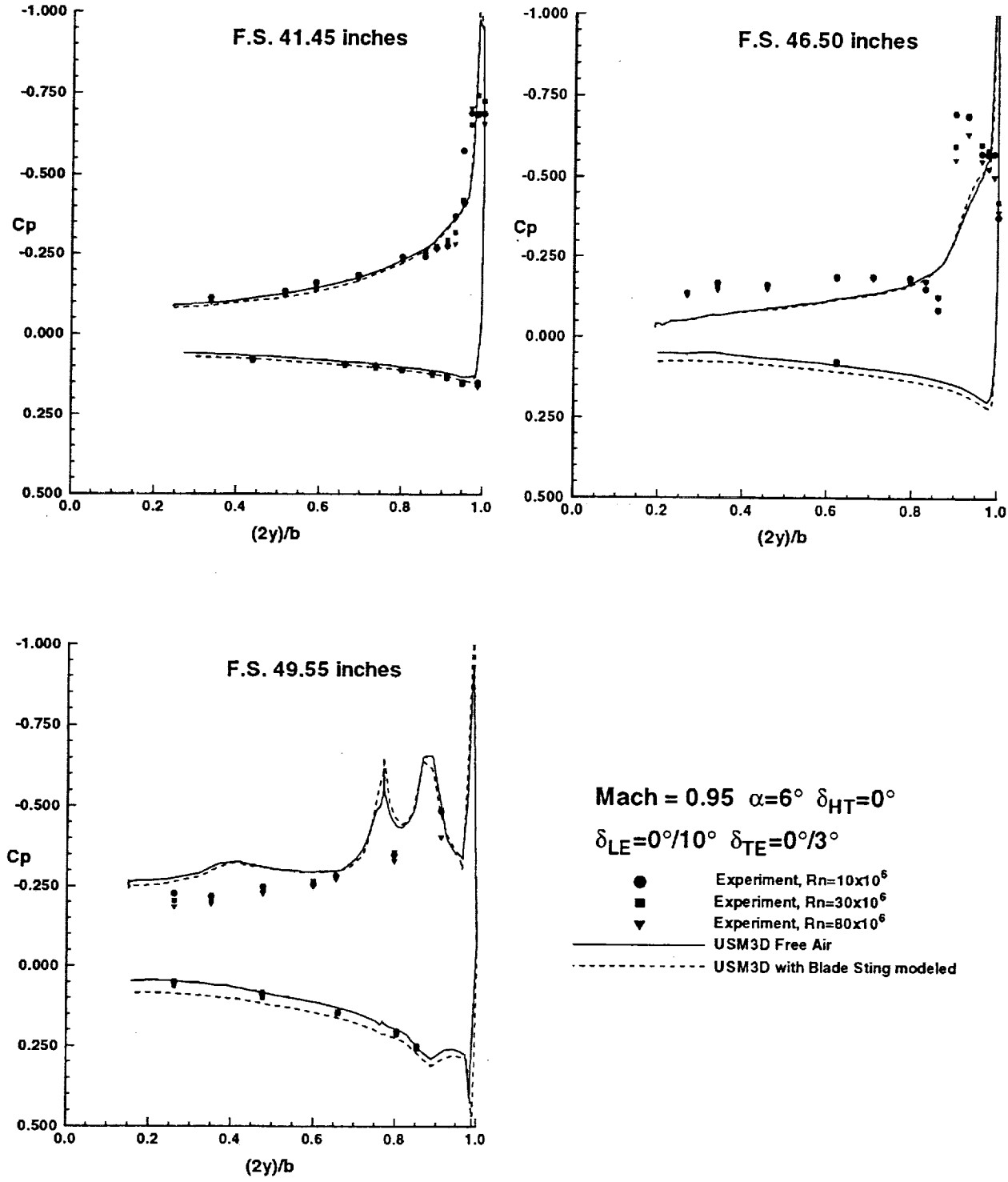

Figure 8. Comparison of predicted and experimental wing surface pressure coefficients; M=0.95, α=6°, δ_{HT}=0°, δ_{LE}=0°/10°, δ_{TE}=0°/3°.

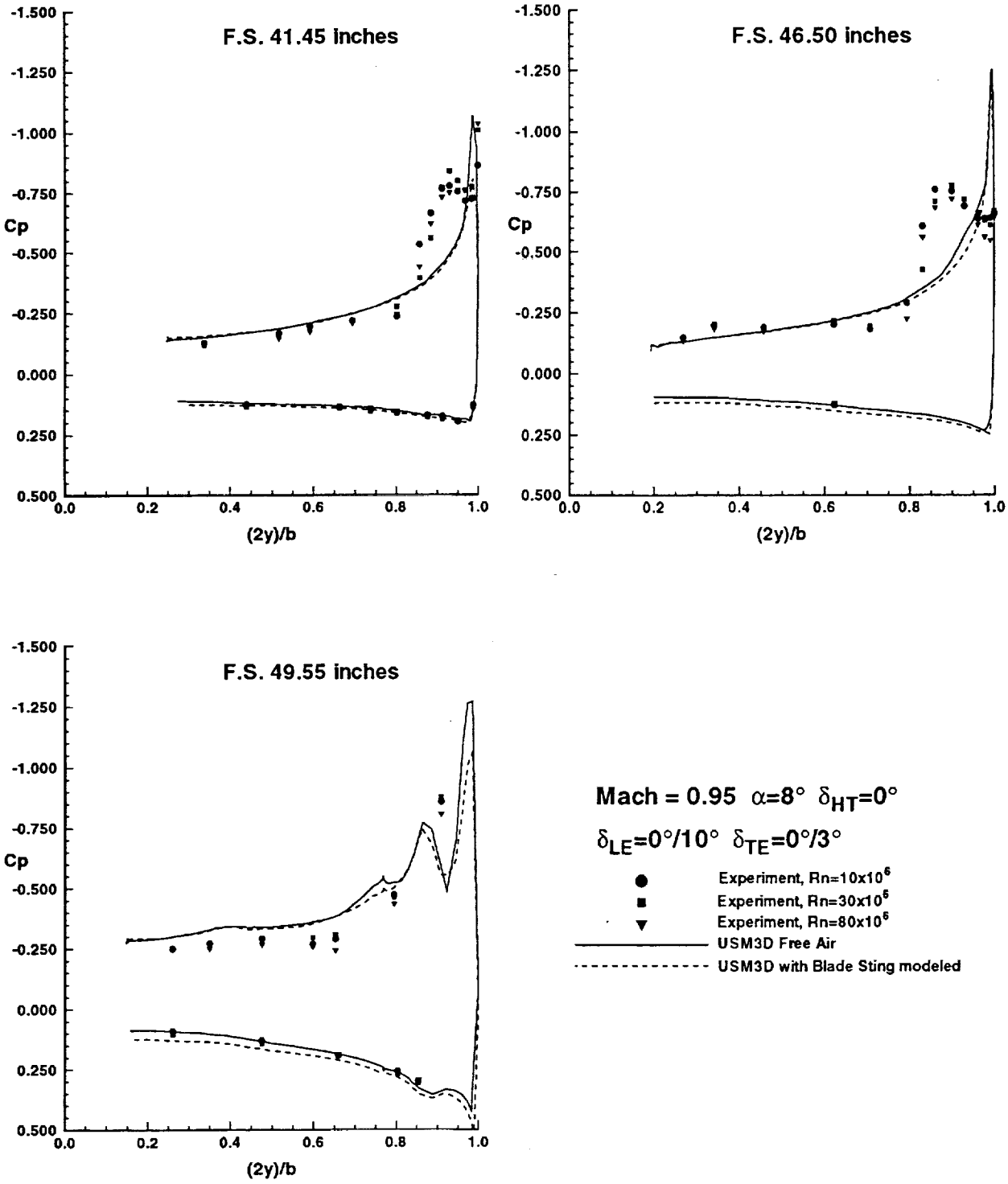

Figure 9. Comparison of predicted and experimental wing surface pressure coefficients; M=0.95, $\alpha=8^{\circ}$, $\delta_{HT}=0^{\circ}$, $\delta_{LE}=0^{\circ}/10^{\circ}$, $\delta_{TE}=0^{\circ}/3^{\circ}$.

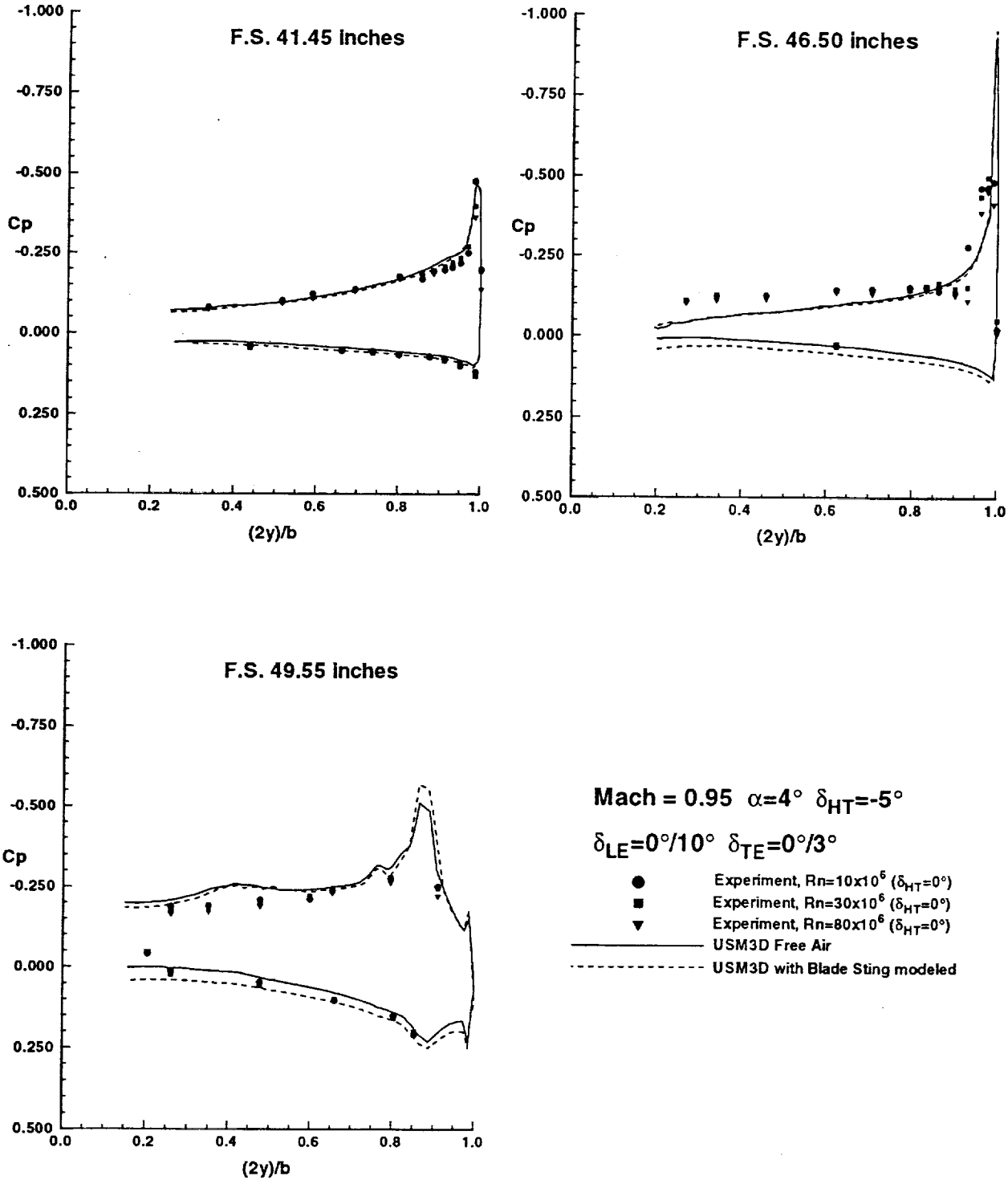

Figure 10. Comparison of predicted and experimental wing surface pressure coefficients; M=0.95, $\alpha=4^{\circ}$, $\delta_{HT}=-5^{\circ}$, $\delta_{LE}=0^{\circ}/10^{\circ}$, $\delta_{TE}=0^{\circ}/3^{\circ}$.

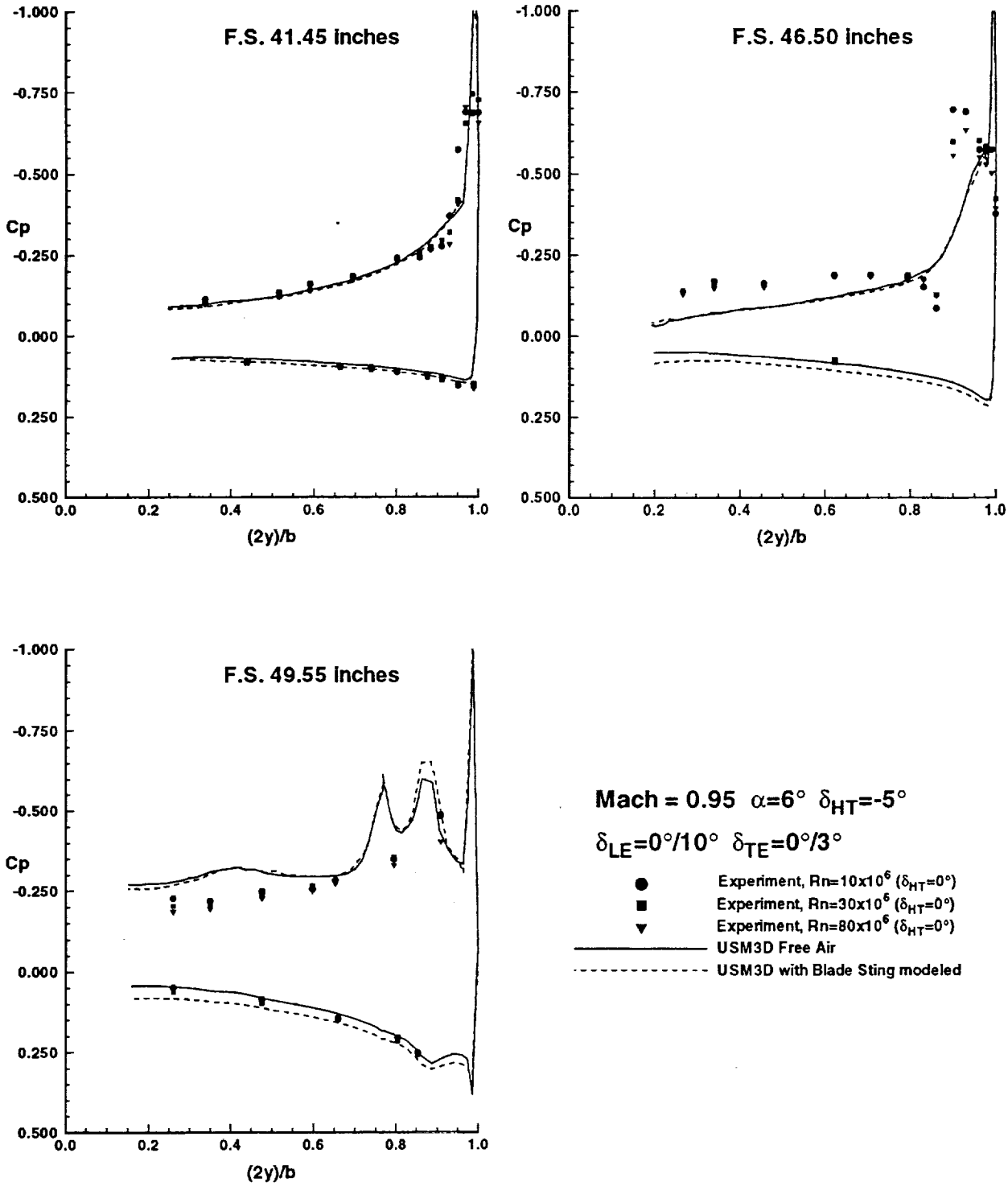

Figure 11. Comparison of predicted and experimental wing surface pressure coefficients; M=0.95, $\alpha=6^{\circ}$, $\delta_{HT}=-5^{\circ}$, $\delta_{LE}=0^{\circ}/10^{\circ}$, $\delta_{TE}=0^{\circ}/3^{\circ}$.

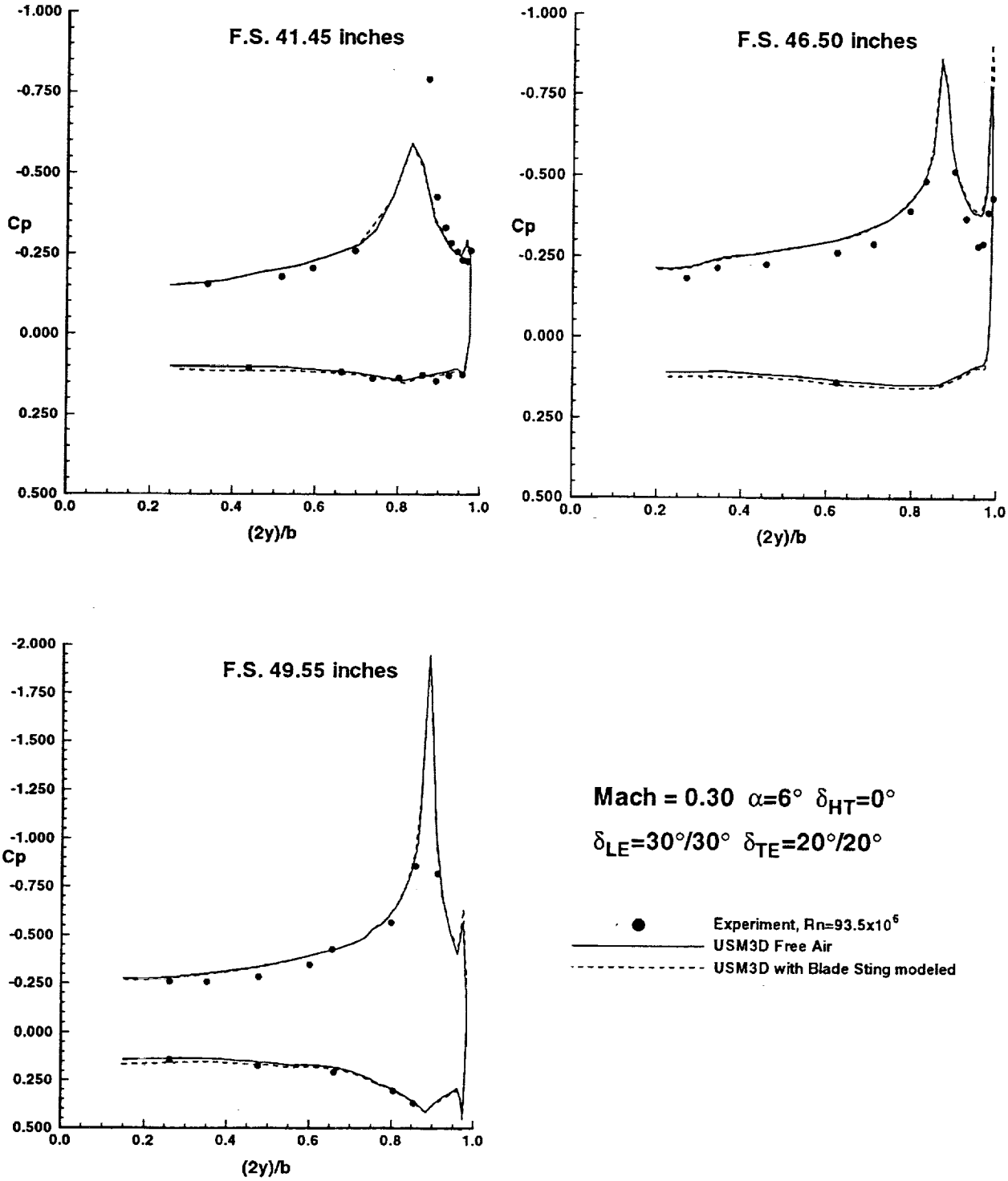

Figure 12. Comparison of predicted and experimental wing surface pressure coefficients; M=0.30, $\alpha=6^{\circ}$, $\delta_{HT}=0^{\circ}$, $\delta_{LE}=30^{\circ}/30^{\circ}$, $\delta_{TE}=20^{\circ}/20^{\circ}$.

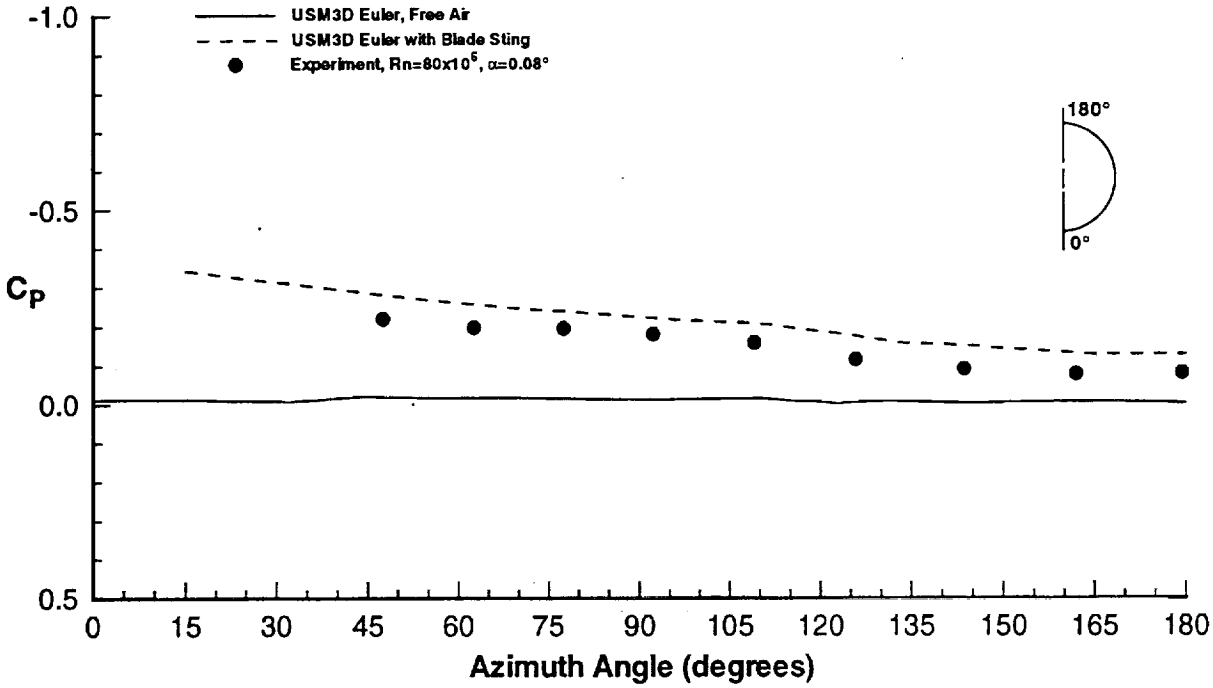

Figure 13. Fuselage pressure coefficient comparison at F.S. 65.306; M=0.95, α=0°, δ_{HT}=0°, δ_{LE}=0°/10°, δ_{TE}=0°/3°.

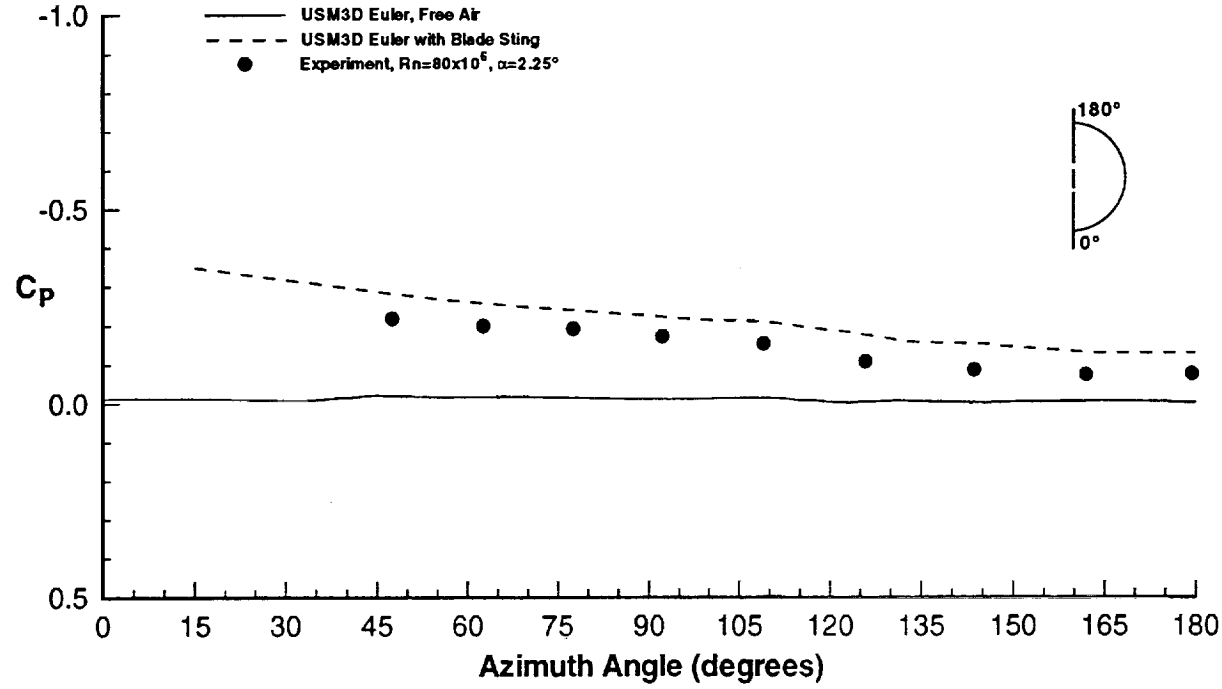

Figure 14. Fuselage pressure coefficient comparison at F.S. 65.306; M=0.95, α=2°, δ_{HT}=0°, δ_{LE}=0°/10°, δ_{TE}=0°/3°.

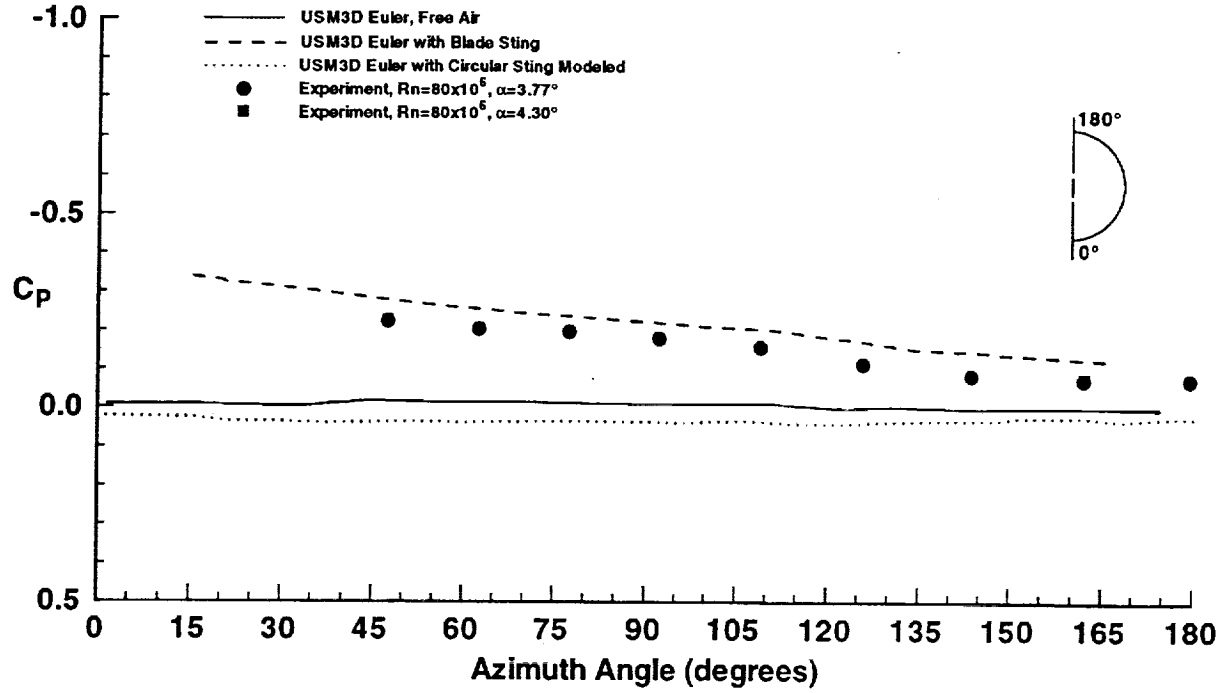

Figure 15. Fuselage pressure coefficient comparison at F.S. 65.306; M=0.95, α=4°, δ_{HT}=0°, δ_{LE}=0°/10°, δ_{TE}=0°/3°.

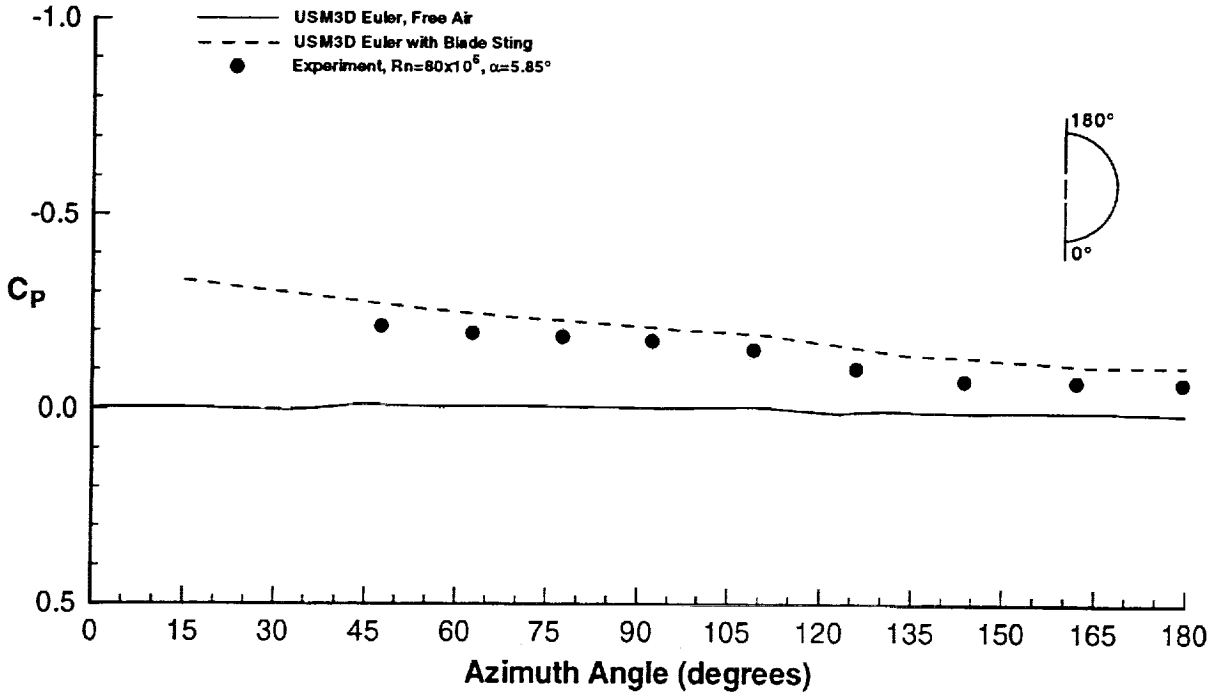

Figure 16. Fuselage pressure coefficient comparison at F.S. 65.306; M=0.95, α=6°, δ_{HT}=0°, δ_{LE}=0°/10°, δ_{TE}=0°/3°.

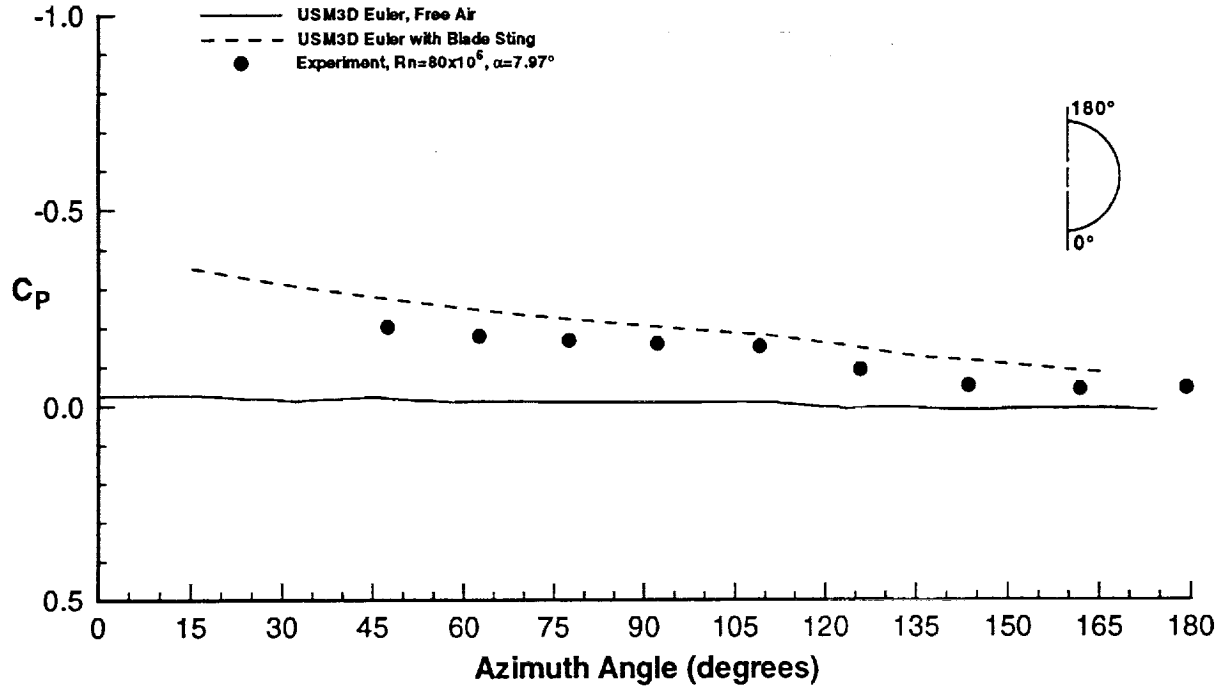

Figure 17. Fuselage pressure coefficient comparison at F.S. 65.306; M=0.95, α=8°, δ_{HT}=0°, δ_{LE}=0°/10°, δ_{TE}=0°/3°.

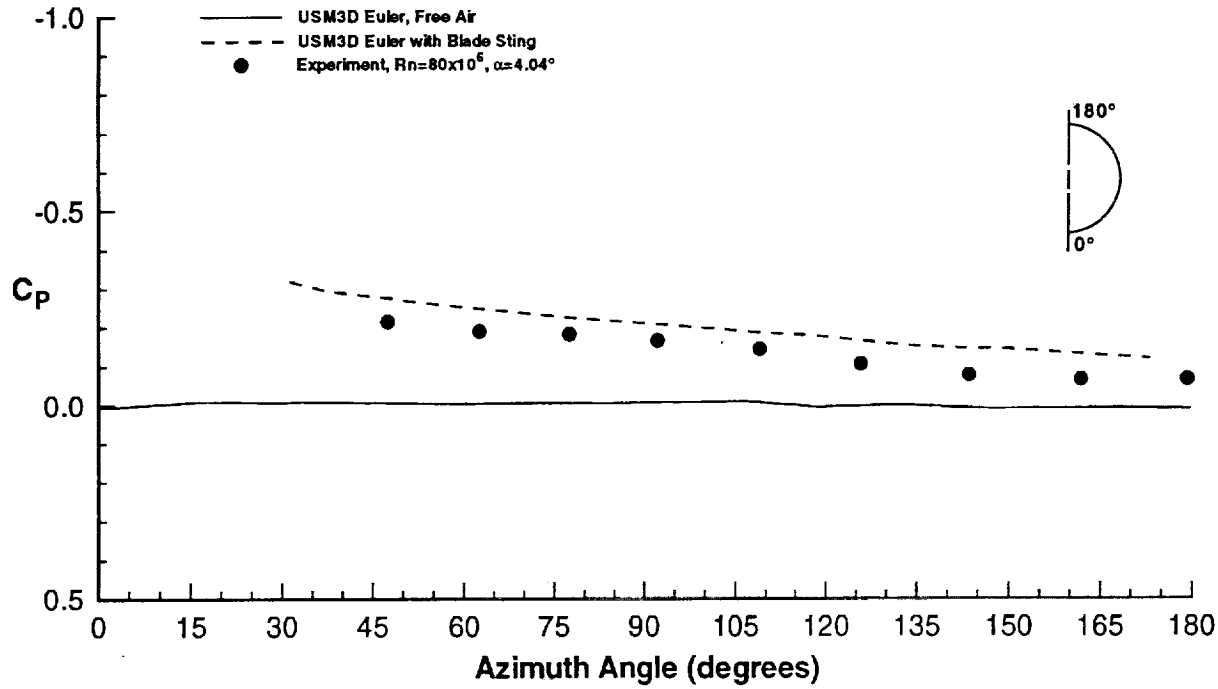

Figure 18. Fuselage pressure coefficient comparison at F.S. 65.306; M=0.95, α=4°, δ_{HT}=-5°, δ_{LE}=0°/10°, δ_{TE}=0°/3°.

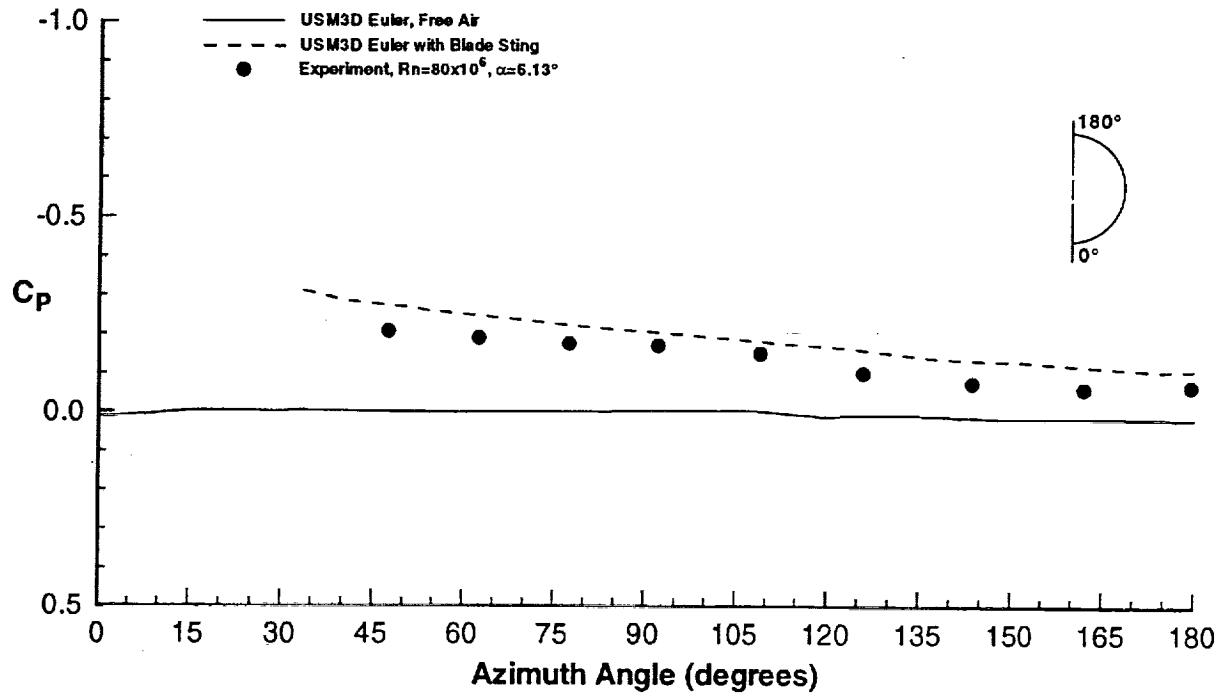

Figure 19. Fuselage pressure coefficient comparison at F.S. 65.306; M=0.95, α=6°, δ_{HT}=-5°, δ_{LE}=0°/10°, δ_{TE}=0°/3°.

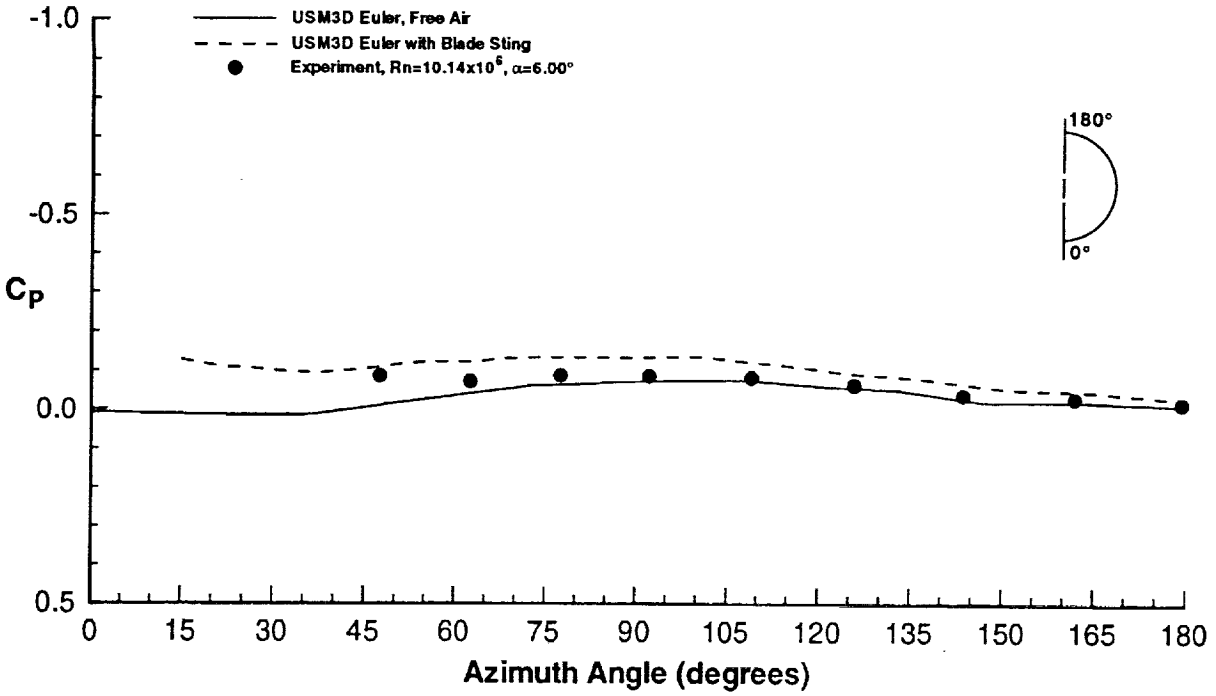

Figure 20. Fuselage pressure coefficient comparison at F.S. 65.306; M=0.30, α=6°, δ_{HT}=0°, δ_{LE}=30°/30°, δ_{TE}=20°/20°.

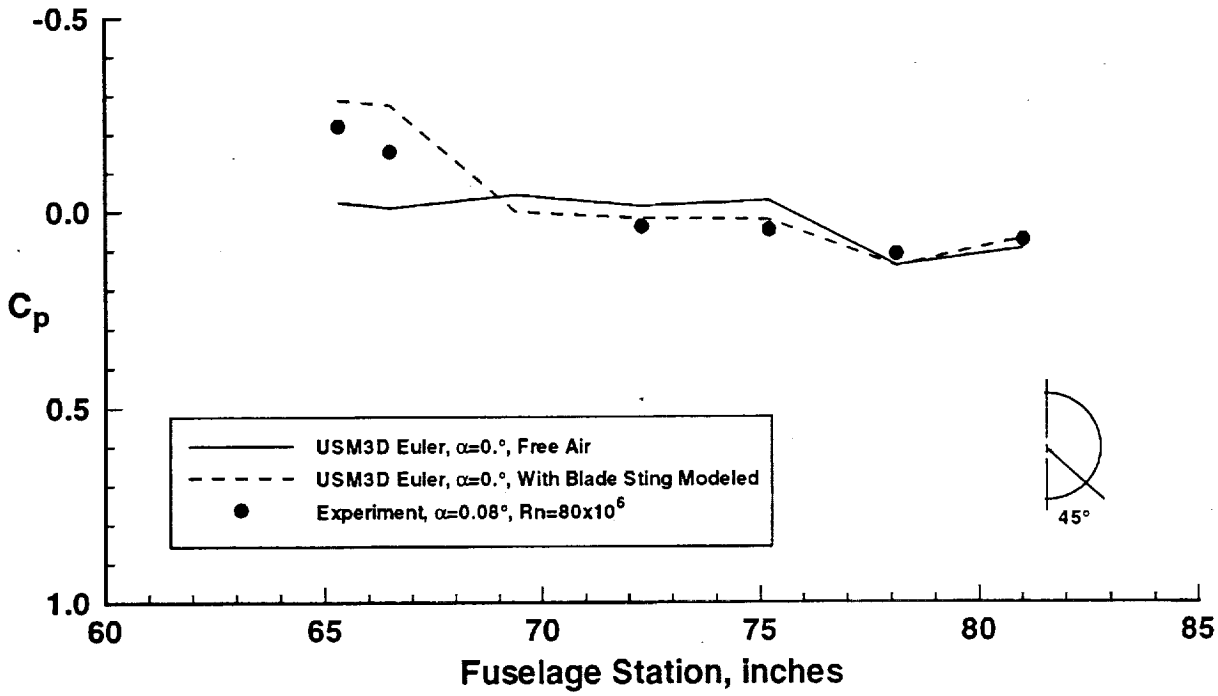

Figure 21. Fuselage pressure coefficient comparison along a line 45° below the horizontal; M=0.95, α=0°, δ_{HT}=0°, δ_{LE}=0°/10°, δ_{TE}=0°/3°.

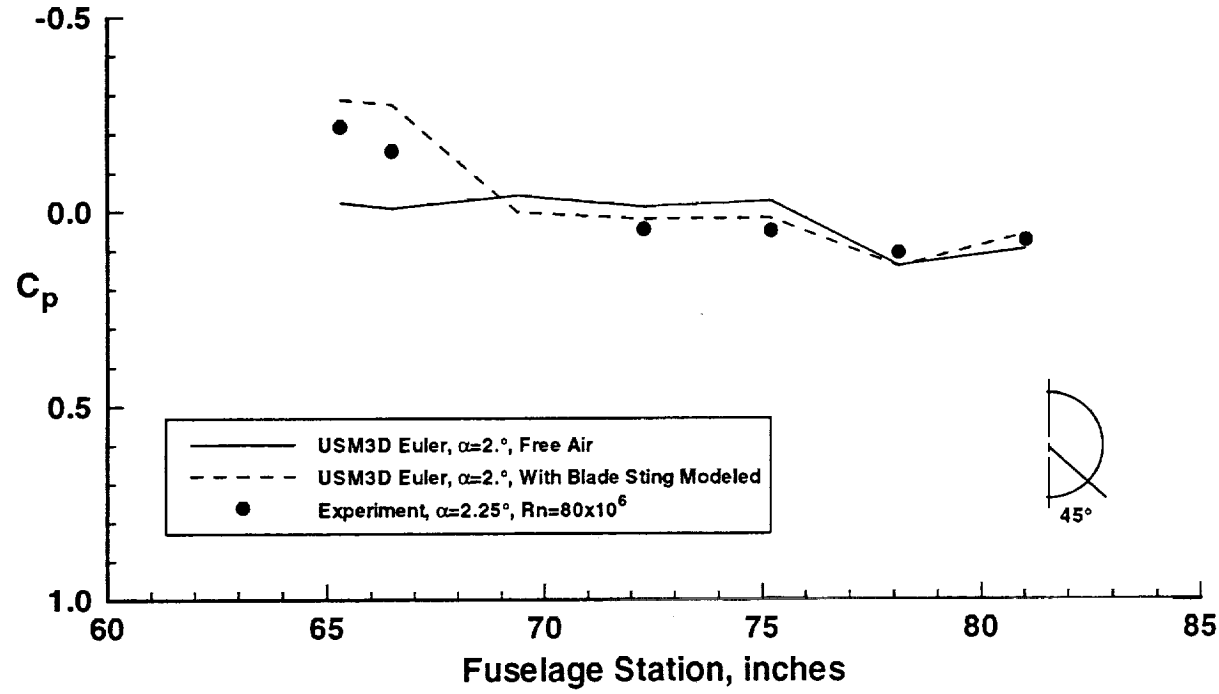

Figure 22. Fuselage pressure coefficient comparison along a line 45° below the horizontal; M=0.95, α=2°, δ_{HT}=0°, δ_{LE}=0°/10°, δ_{TE}=0°/3°.

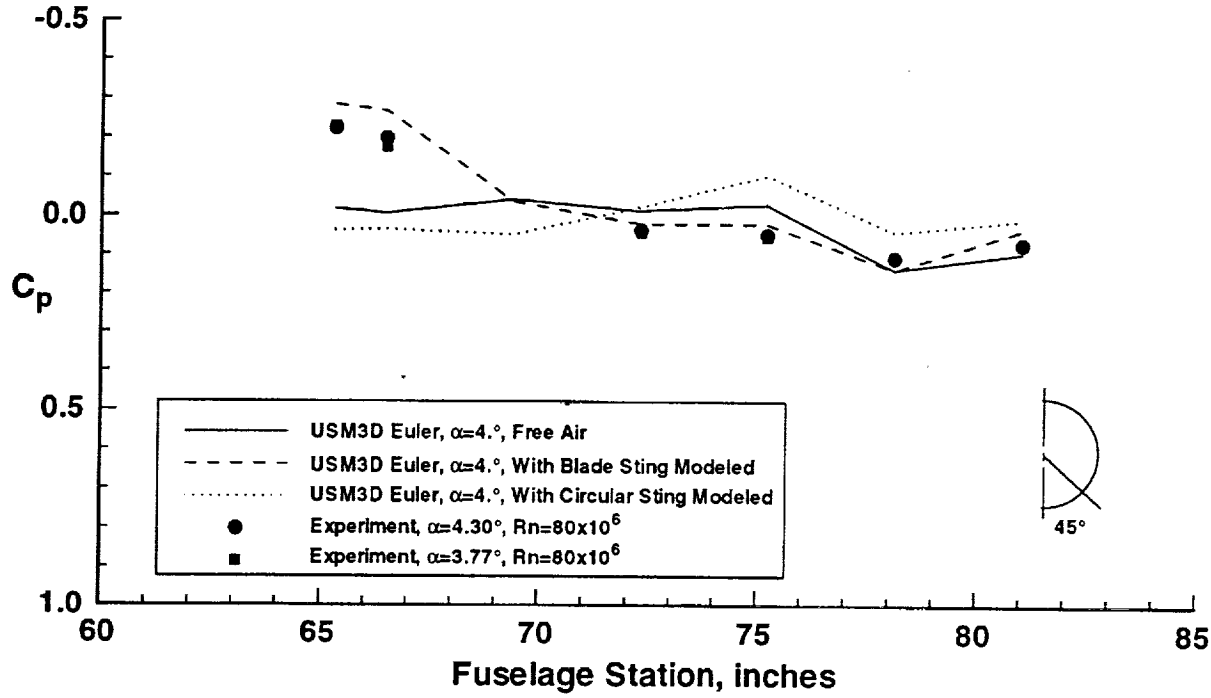

Figure 23. Fuselage pressure coefficient comparison along a line 45° below the horizontal; M=0.95, α=4°, δ_{HT}=0°, δ_{LE}=0°/10°, δ_{TE}=0°/3°.

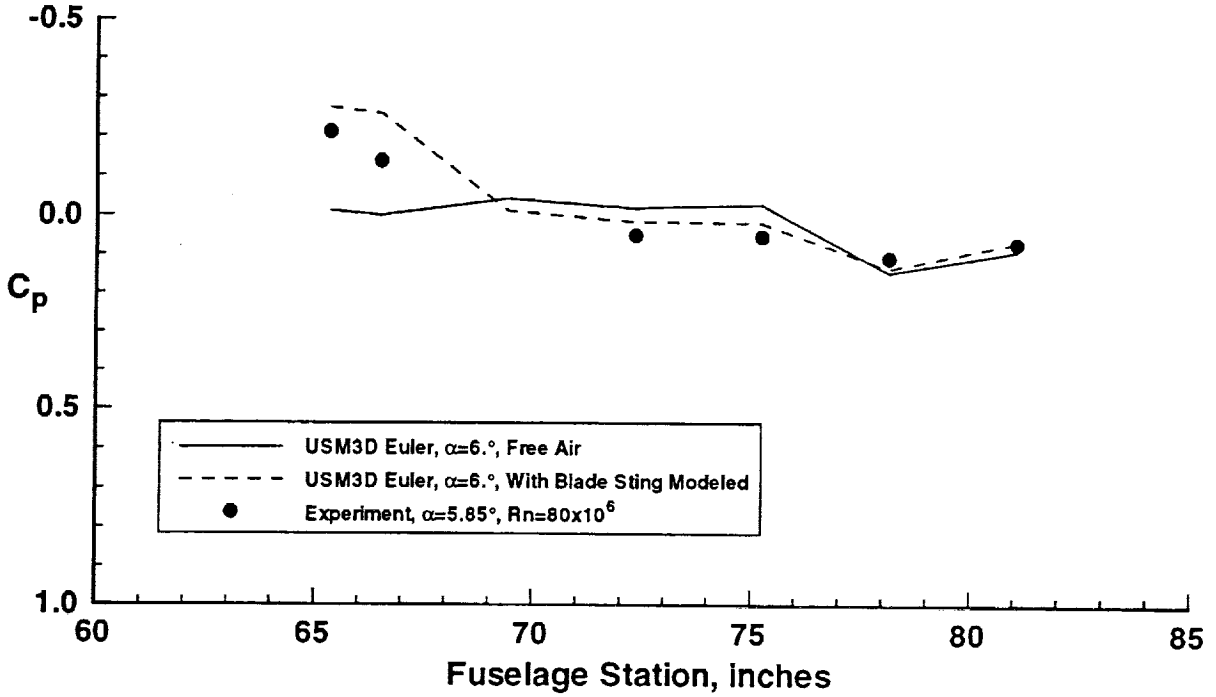

Figure 24. Fuselage pressure coefficient comparison along a line 45° below the horizontal; M=0.95, α=6°, δ_{HT}=0°, δ_{LE}=0°/10°, δ_{TE}=0°/3°.

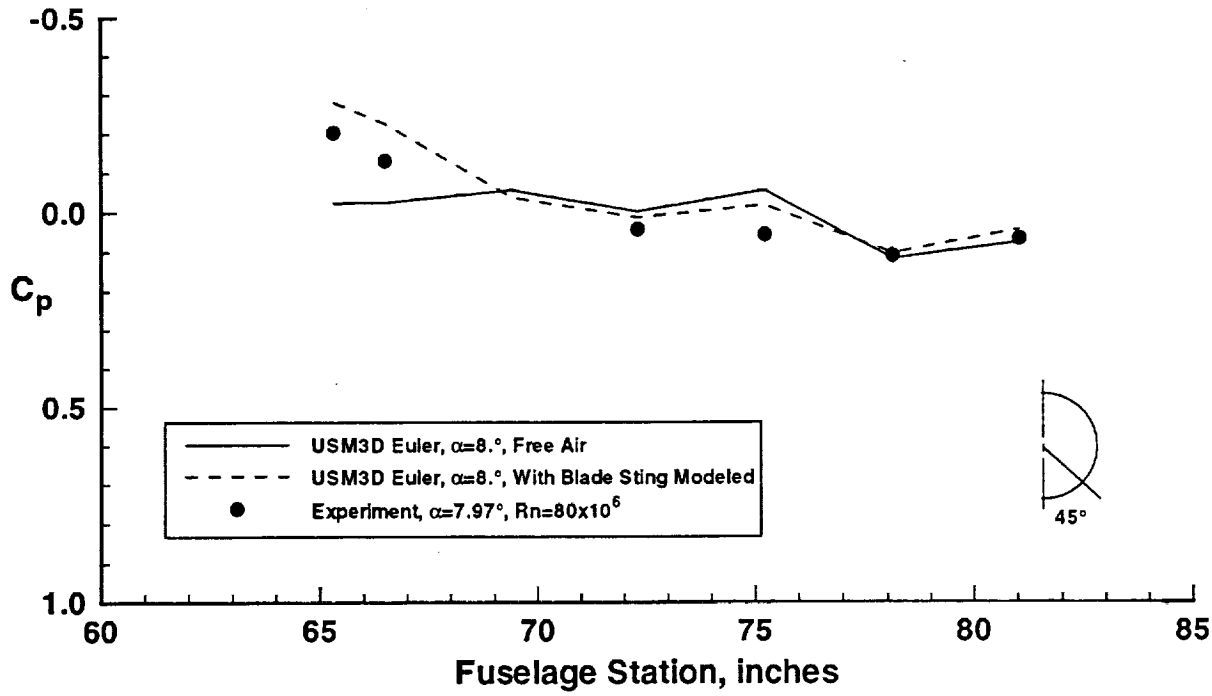

Figure 25. Fuselage pressure coefficient comparison along a line 45° below the horizontal; M=0.95, α=8°, δ_{HT}=0°, δ_{LE}=0°/10°, δ_{TE}=0°/3°.

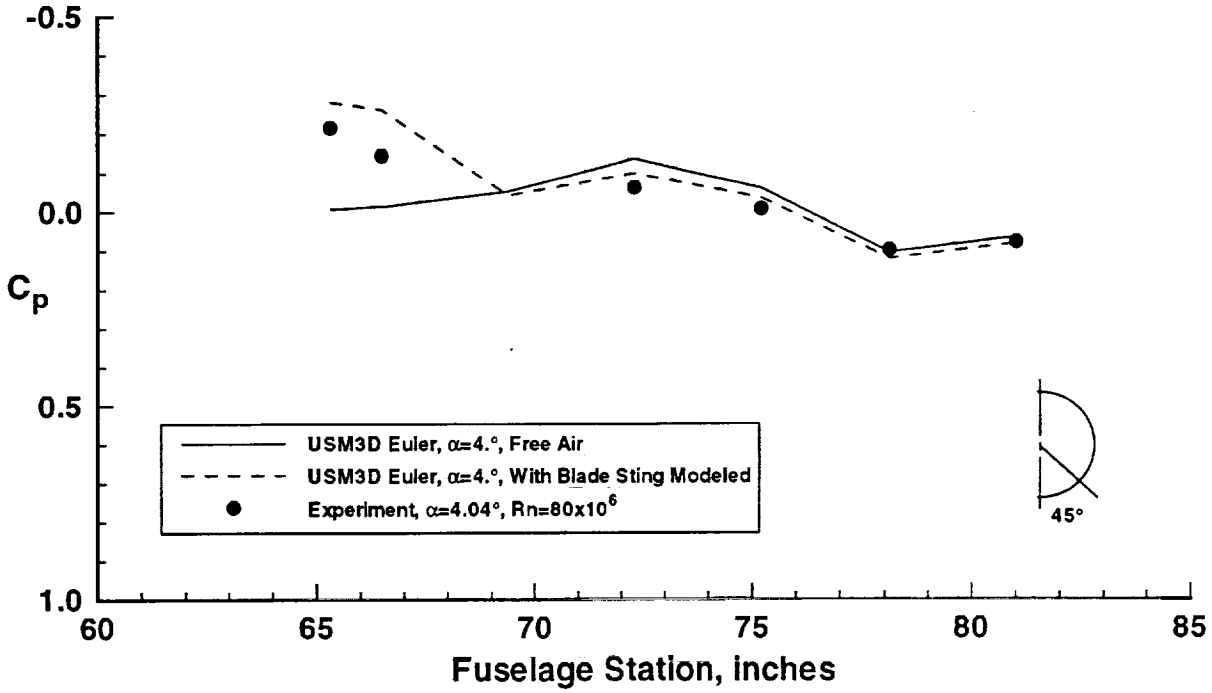

Figure 26. Fuselage pressure coefficient comparison along a line 45° below the horizontal; M=0.95, α=4°, δ_{HT}=-5°, δ_{LE}=0°/10°, δ_{TE}=0°/3°.

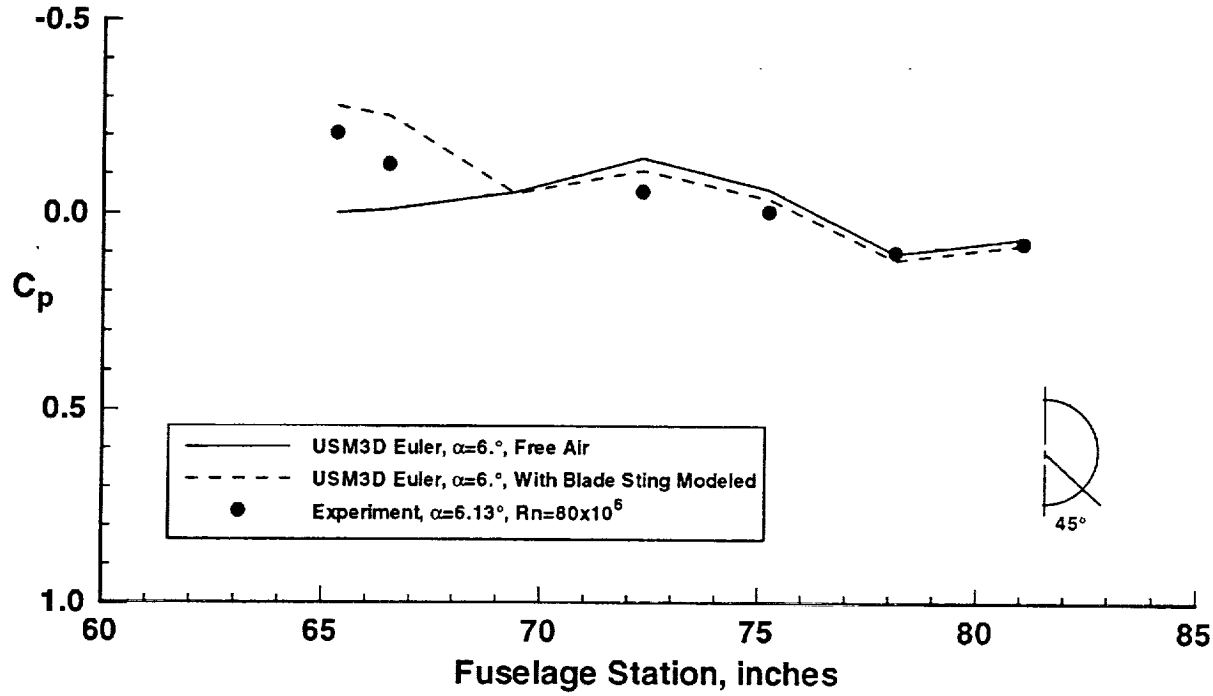

Figure 27. Fuselage pressure coefficient comparison along a line 45° below the horizontal; M=0.95, α=6°, δ_{HT}=-5°, δ_{LE}=0°/10°, δ_{TE}=0°/3°.

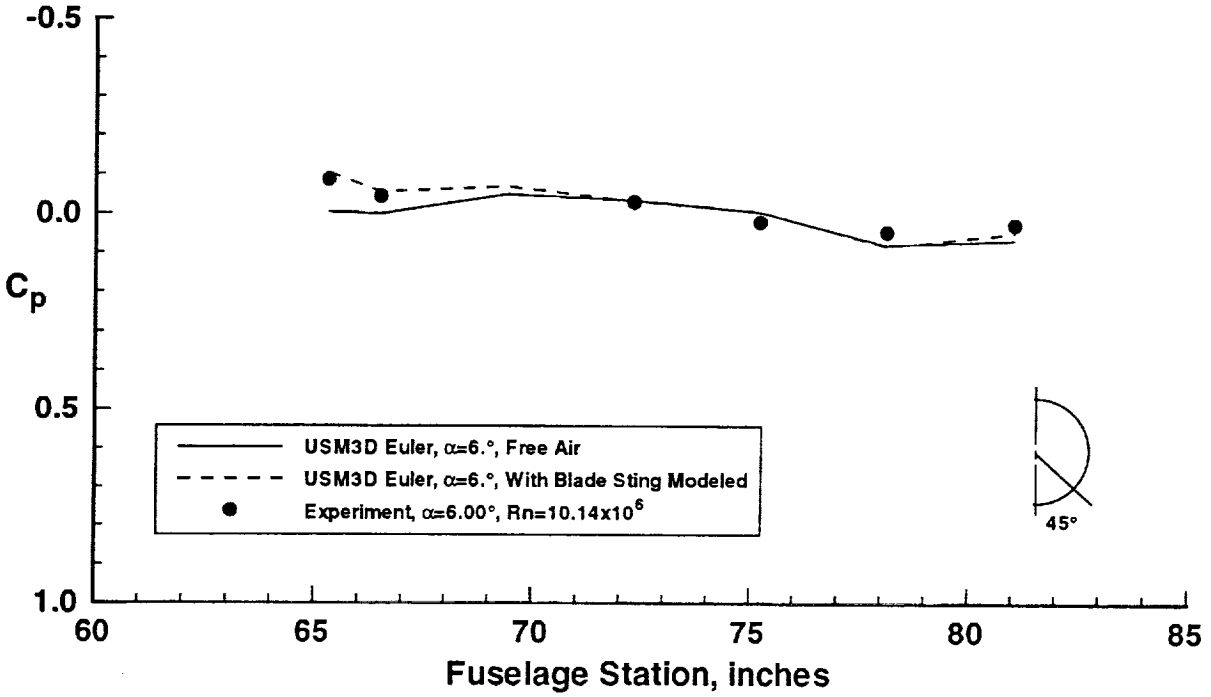

Figure 28. Fuselage pressure coefficient comparison along a line 45° below the horizontal; M=0.30, α=6°, δ_{HT}=0°, δ_{LE}=30°/30°, δ_{TE}=20°/20°.

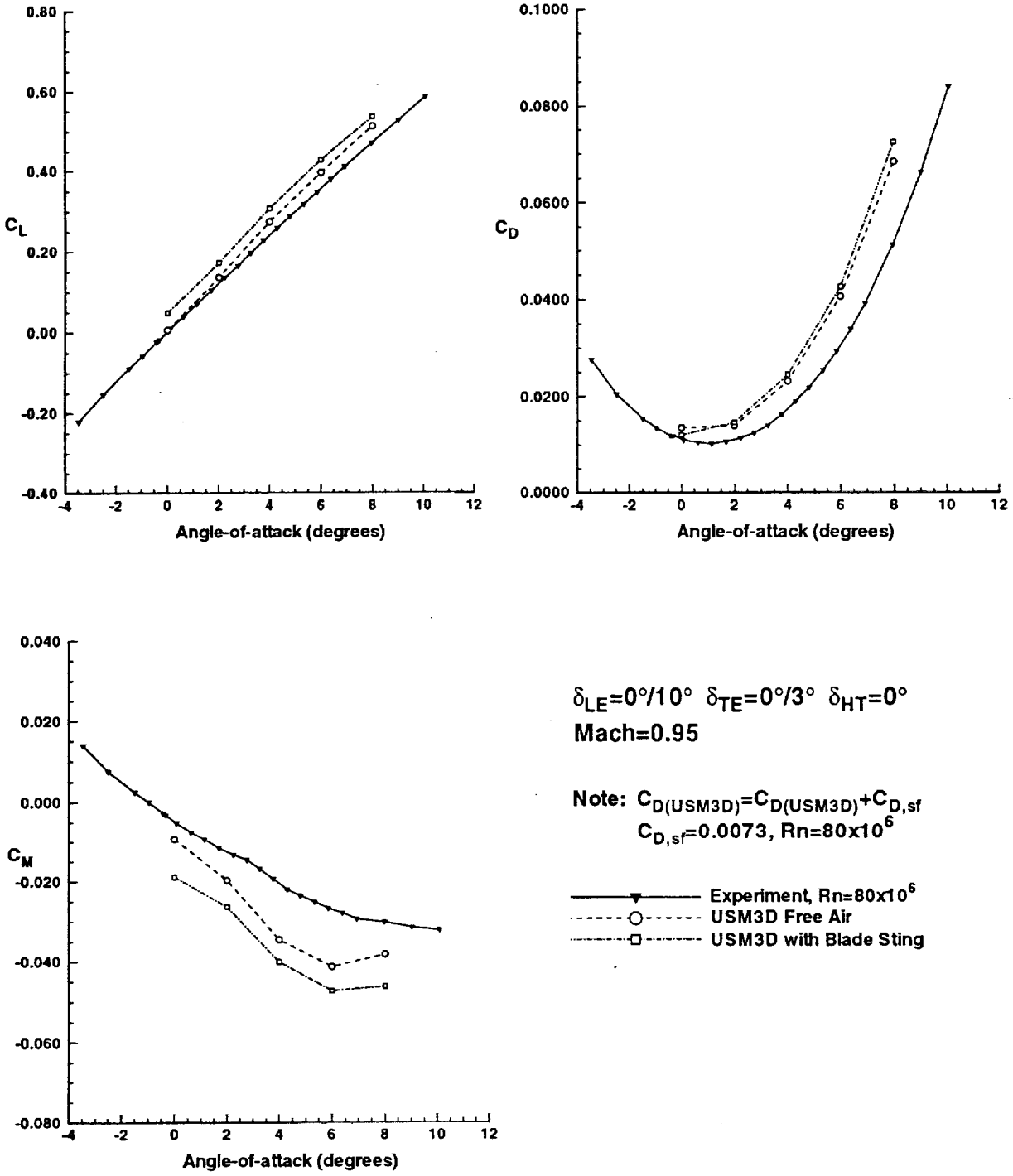

Figure 29. Comparison of predicted and experimental forces and moment.

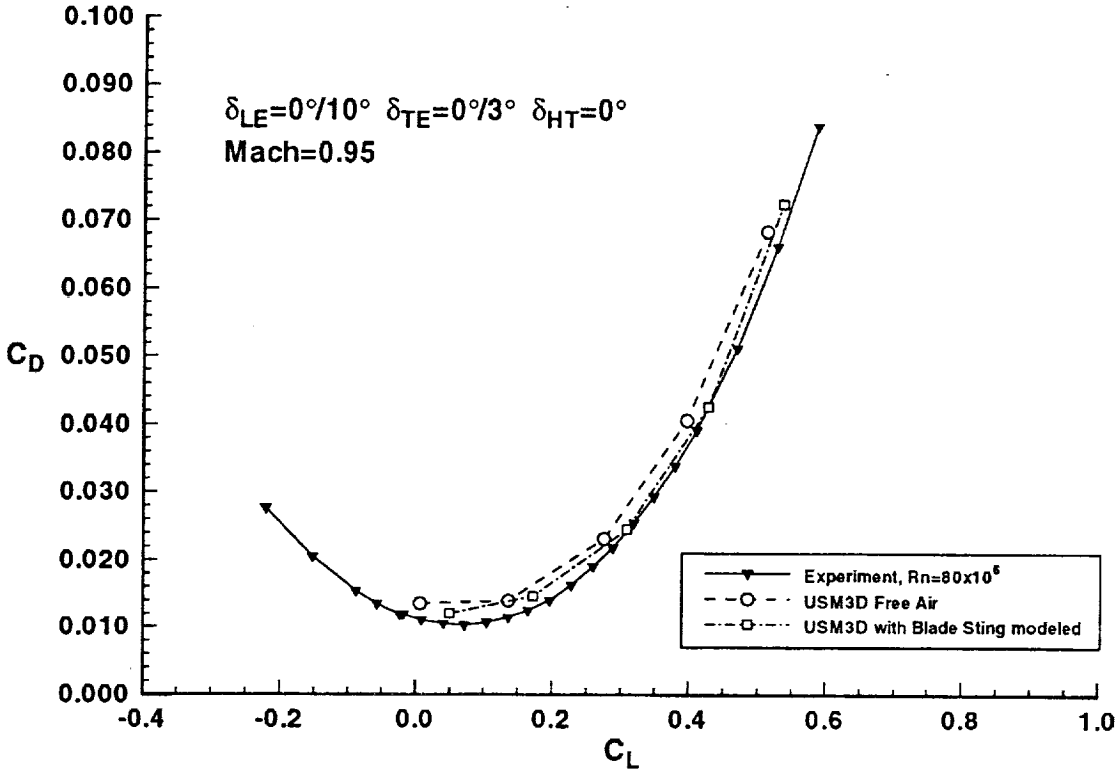

Figure 30. Comparison of predicted and experimental drag polars.

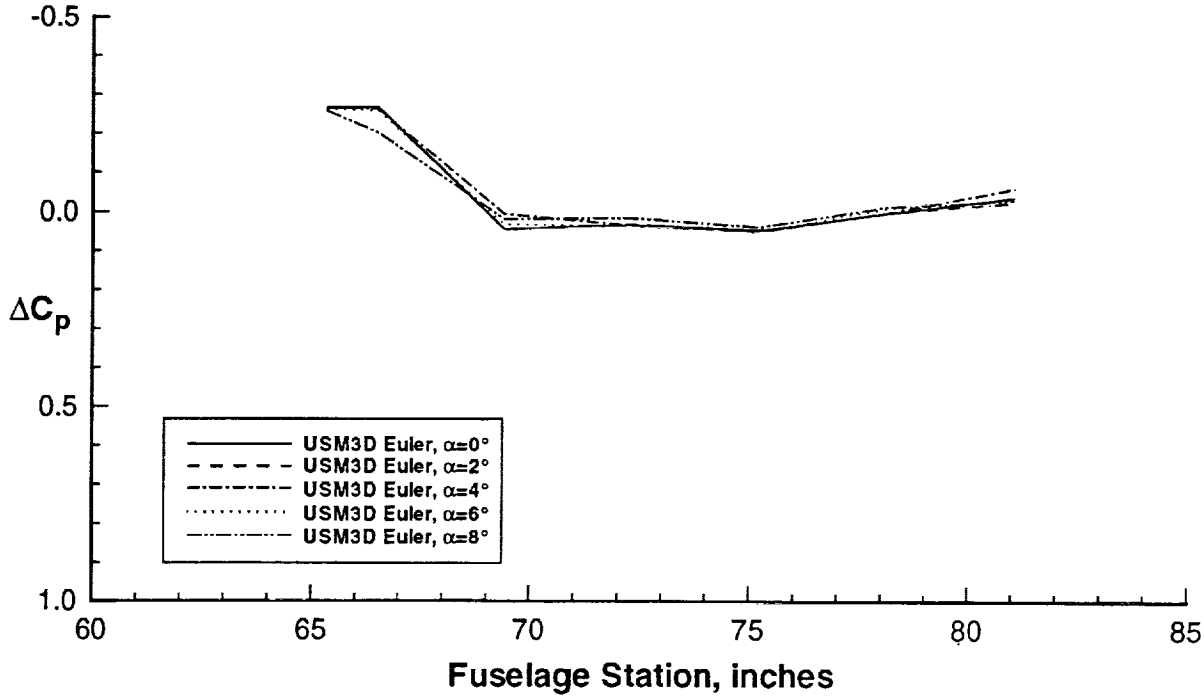

Figure 31. Fuselage pressure coefficient increment due to blade sting comparison along a line 45° below the horizontal; M=0.95, δ_{HT}=0°, δ_{LE}=0°/10°, δ_{TE}=0°/3°

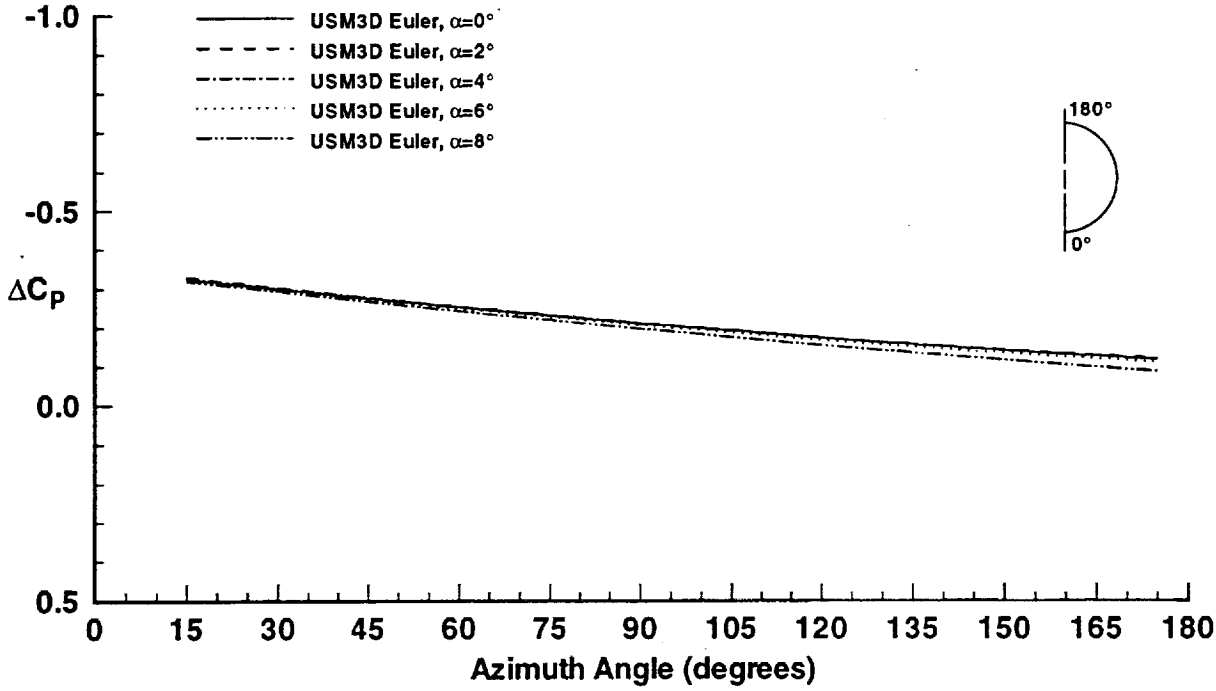

Figure 32. Predicted fuselage pressure coefficients at F.S. 65.306; M=0.95, $\delta_{HT}=0^{\circ}$, $\delta_{LE}=0^{\circ}/10^{\circ}$, $\delta_{TE}=0^{\circ}/3^{\circ}$

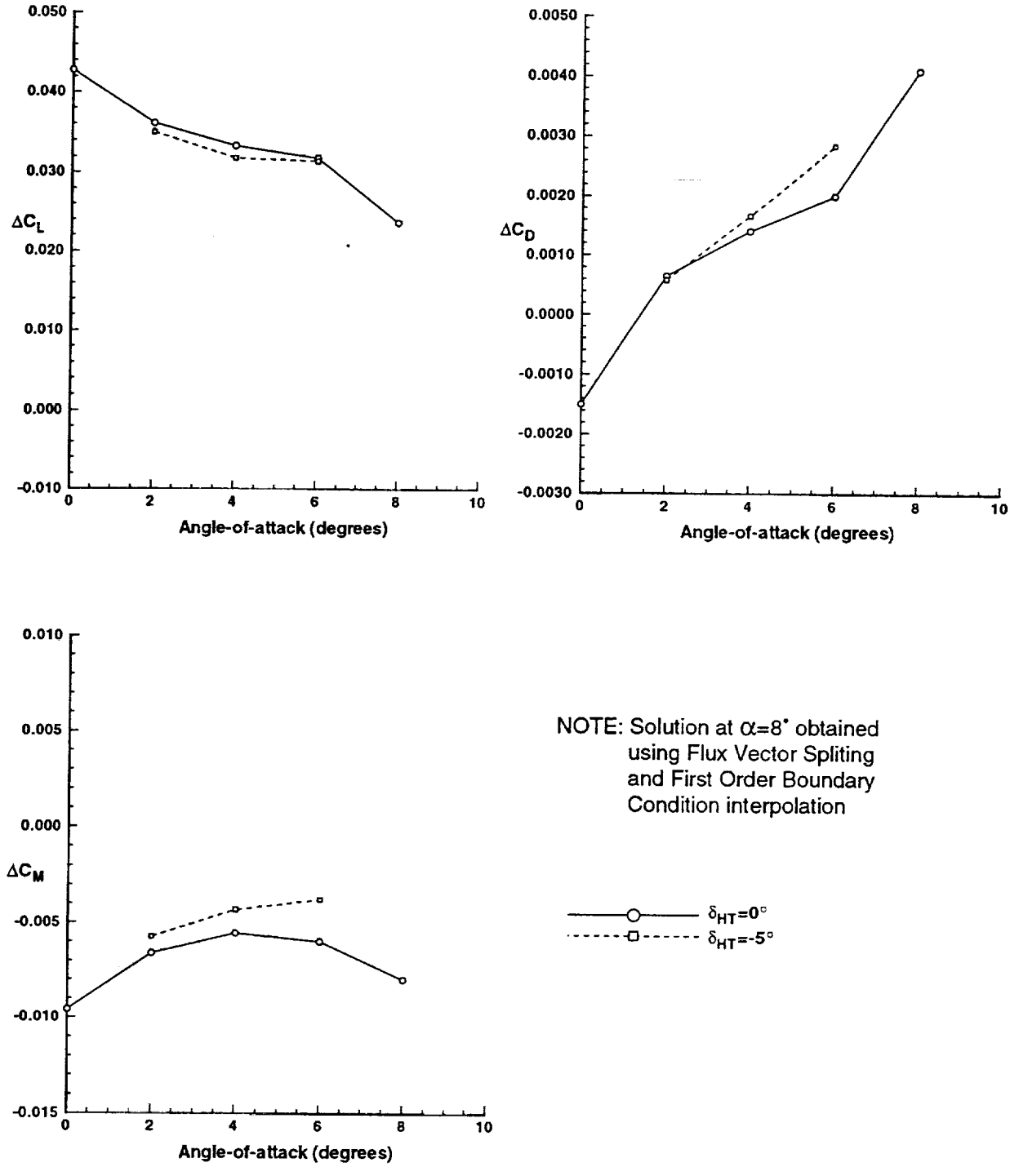

Figure 33. Predicted force and moment increments due to blade sting; M=0.95, δ_{LE}=0°/10°, δ_{TE}=0°/3°.

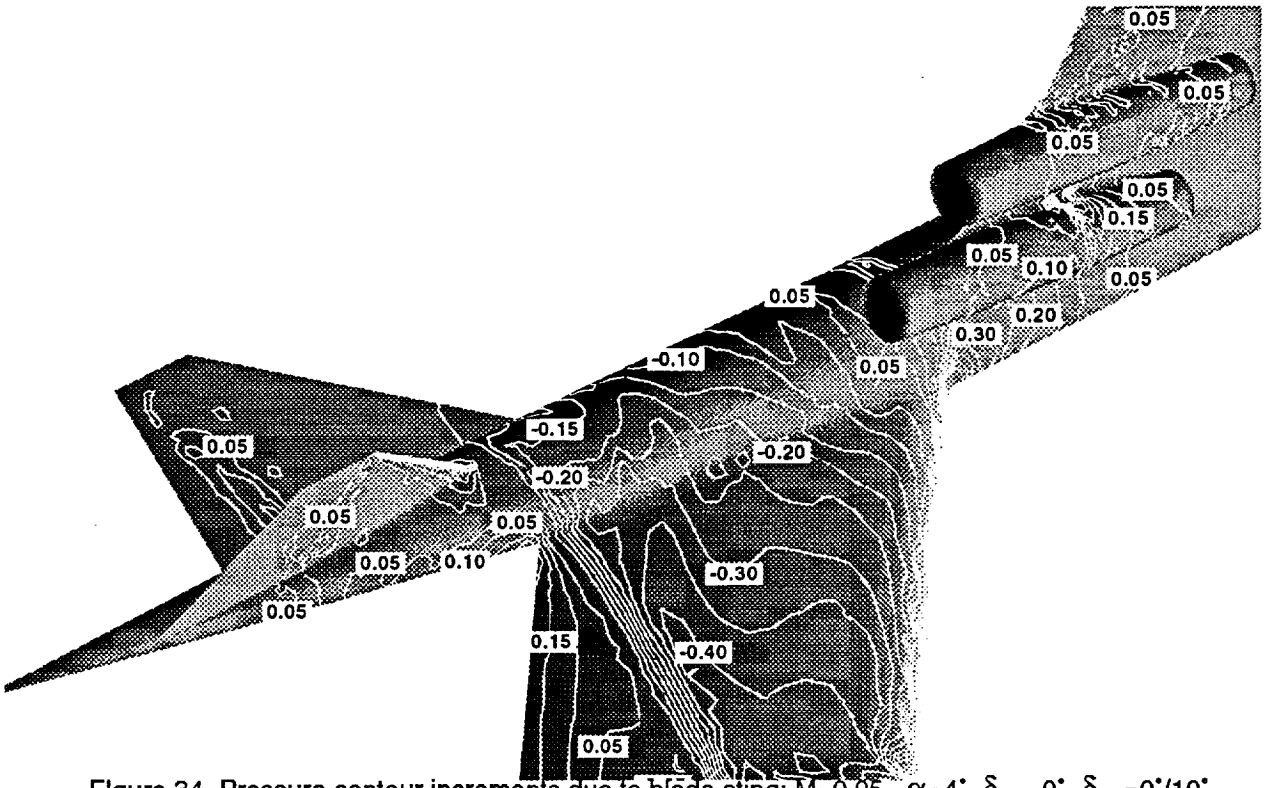

Figure 34. Pressure contour increments due to blade sting; M=0.95, α=4°, δ_{HT}=0°, δ_{LE}=0°/10°, δ_{TE}=0°/3°, (ΔC_p=0.05).

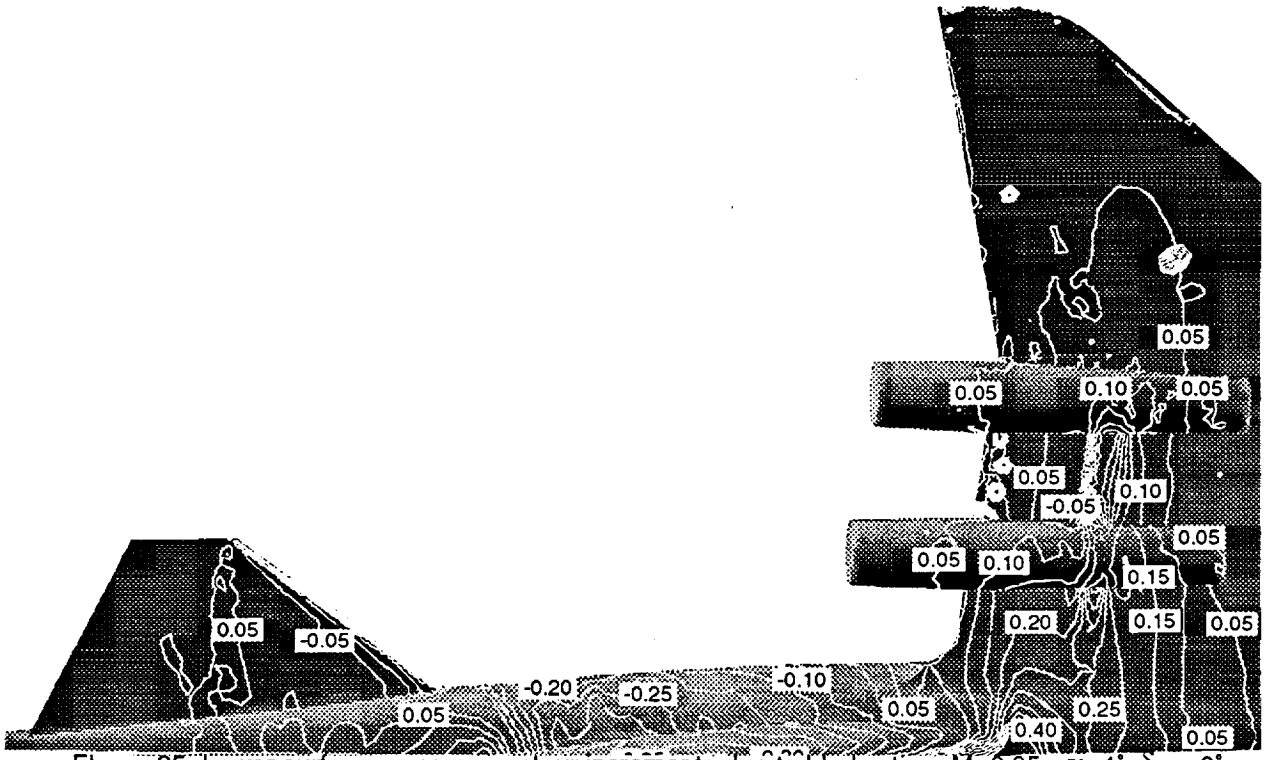

Figure 35. Lower surface pressure contour increments due to blade sting; M=0.95, α=4°, δ_{HT}=0°, δ_{LE}=0°/10°, δ_{TE}=0°/3°, (ΔC_p=0.05).

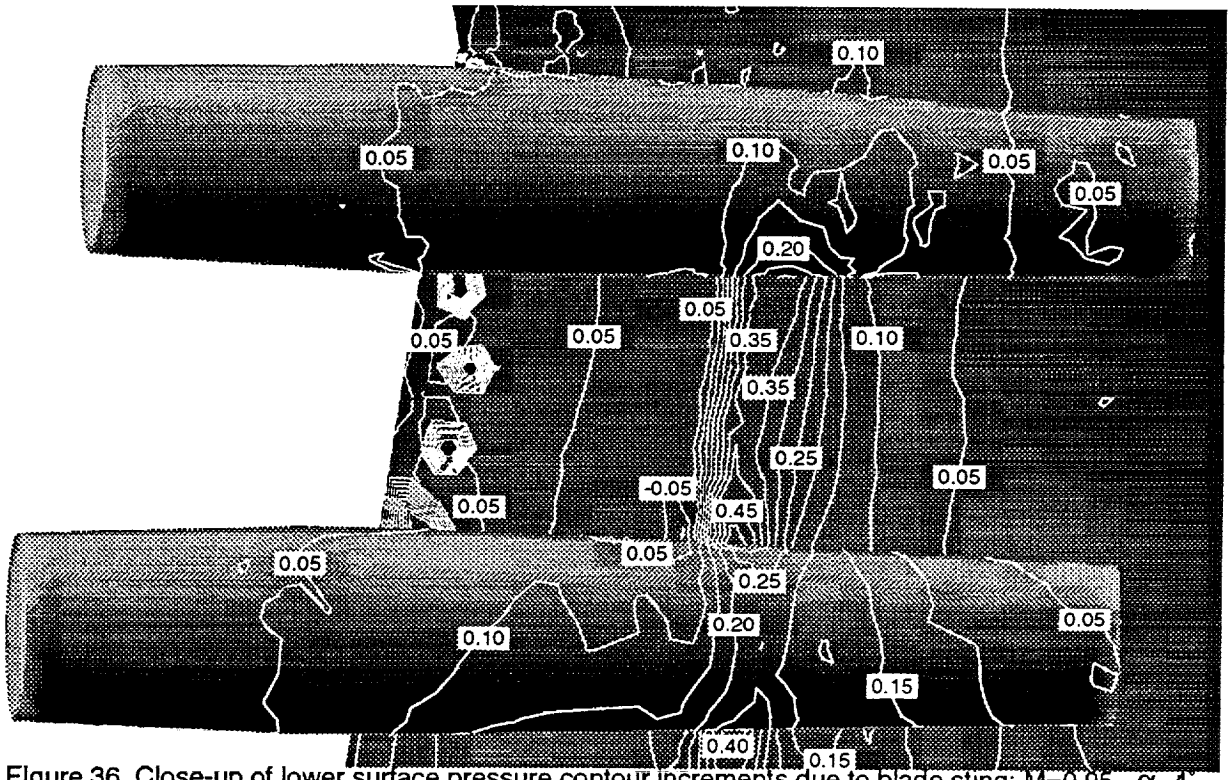

FIgure 36. Close-up of lower surface pressure contour increments due to blade sting; M=0.95, α=4°, δ_{HT}=0°, δ_{LE}=0°/10°, δ_{TE}=0°/3°, (ΔC_p=0.05).

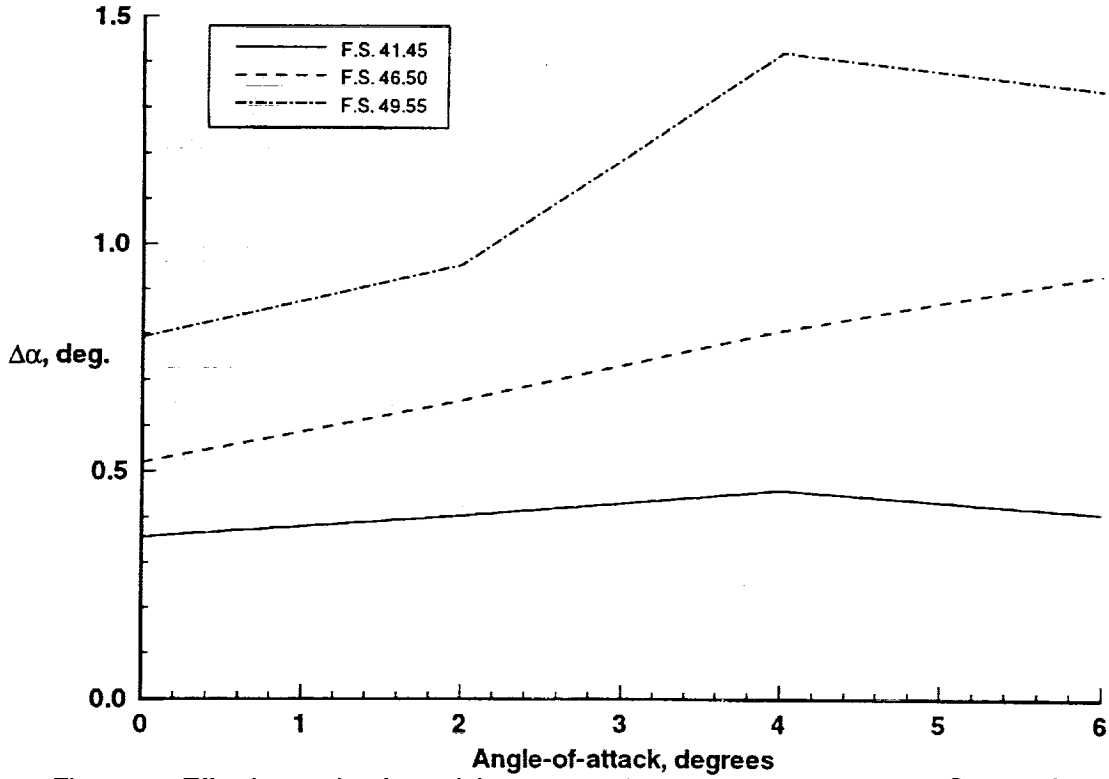

FIgure 37. Effective angle-of-attack increments due to blade sting; M=0.95, δ_{HT}=0°, δ_{LE}=0°/10°, δ_{TE}=0°/3°, (ΔC_p=0.05).

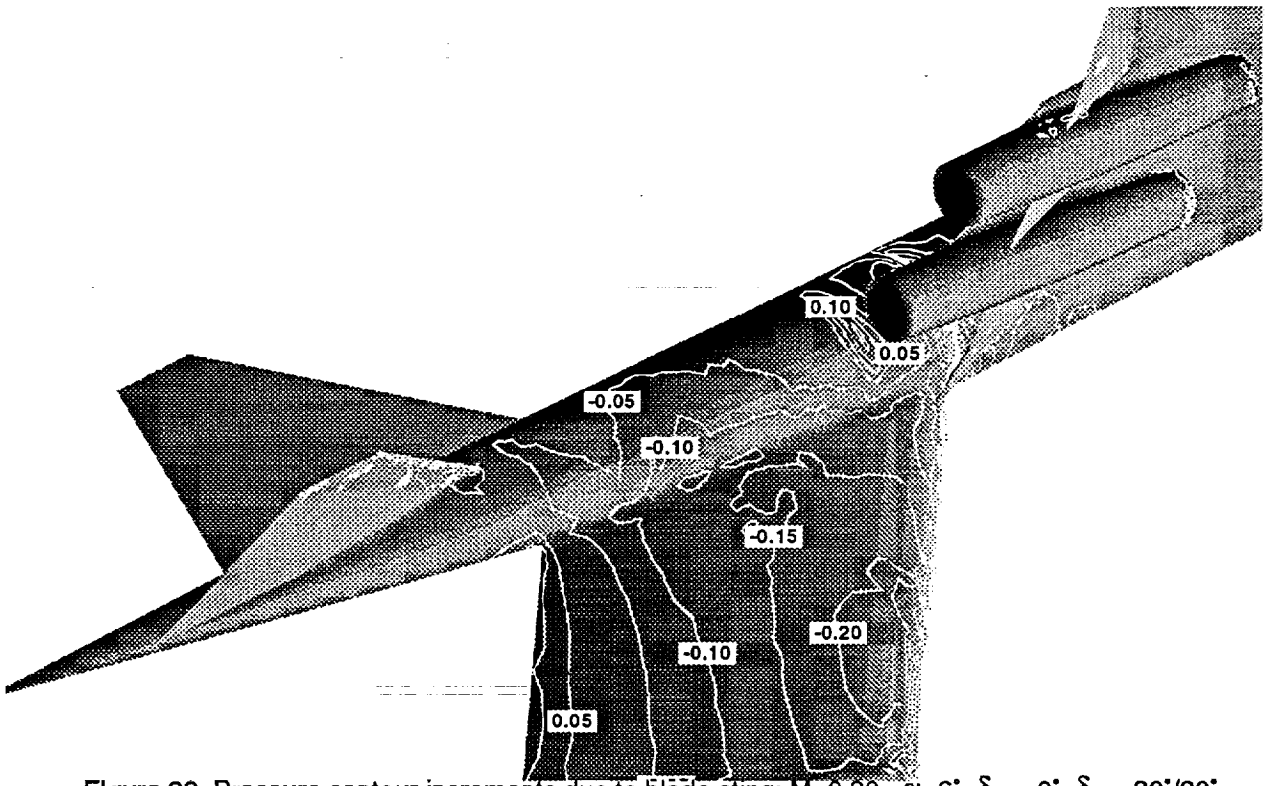

Figure 38. Pressure contour increments due to blade sting; M=0.30, α=6°, δ_{HT}=0°, δ_{LE}=30°/30°, δ_{TE}=20°/20°, (ΔC_p=0.05).

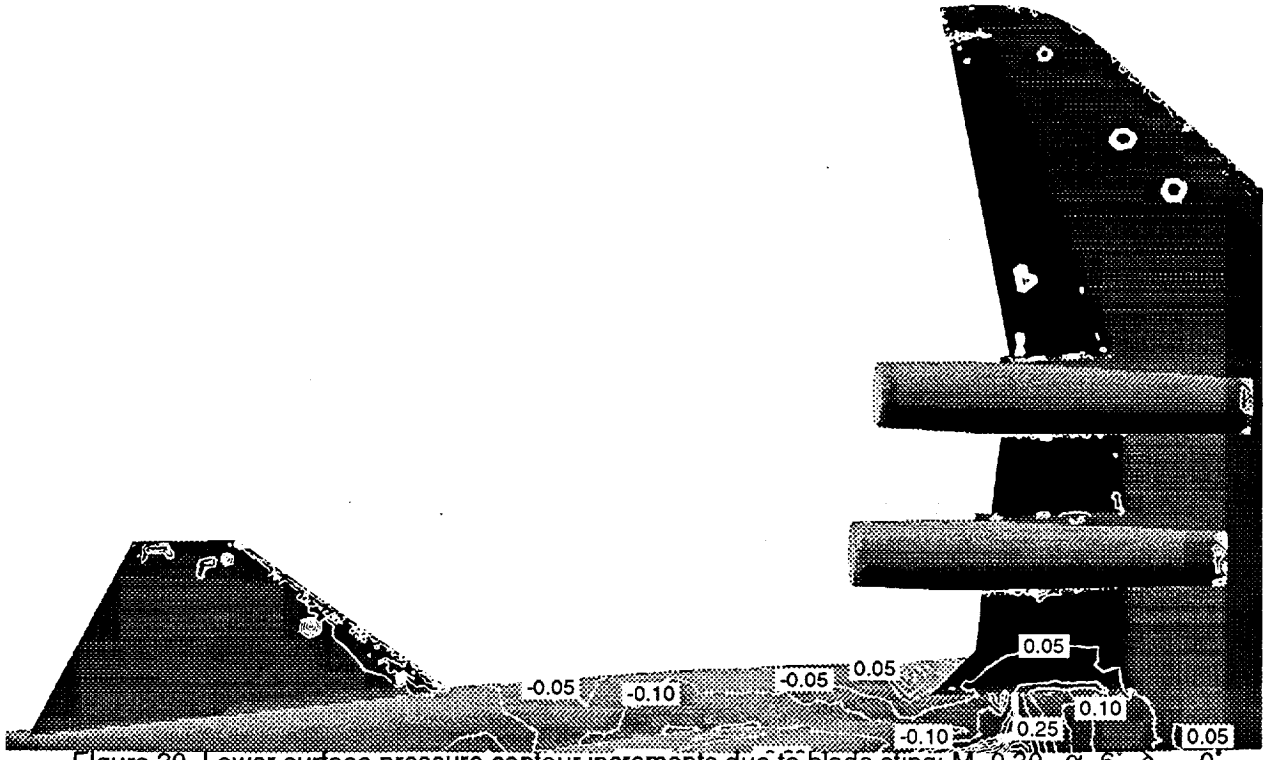

Figure 39. Lower surface pressure contour increments due to blade sting; M=0.30, α=6°, δ_{HT}=0°, δ_{LE}=30°/30°, δ_{TE}=20°/20°, (ΔC_p=0.05).

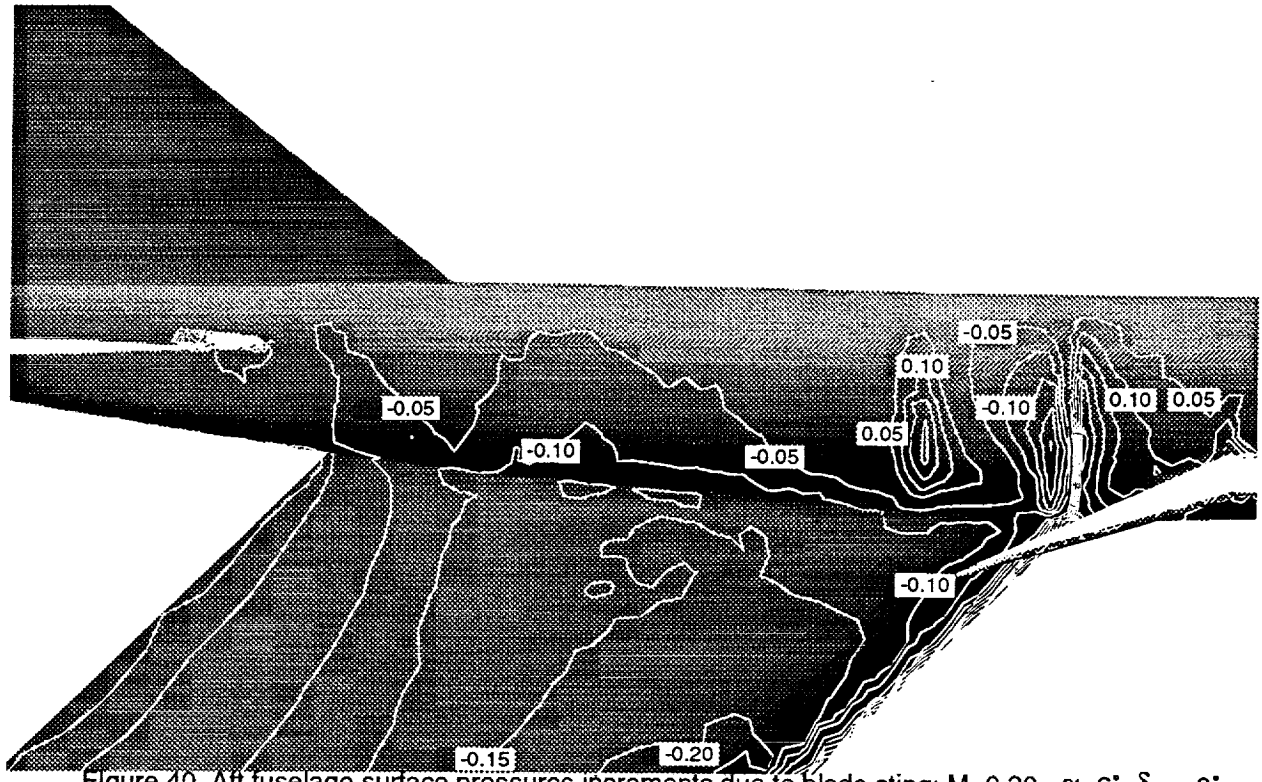

Figure 40. Aft fuselage surface pressures increments due to blade sting; M=0.30, α=6°, δ_{HT}=0°, δ_{LE}=30°/30°, δ_{TE}=20°/20°, (ΔC_p=0.05).

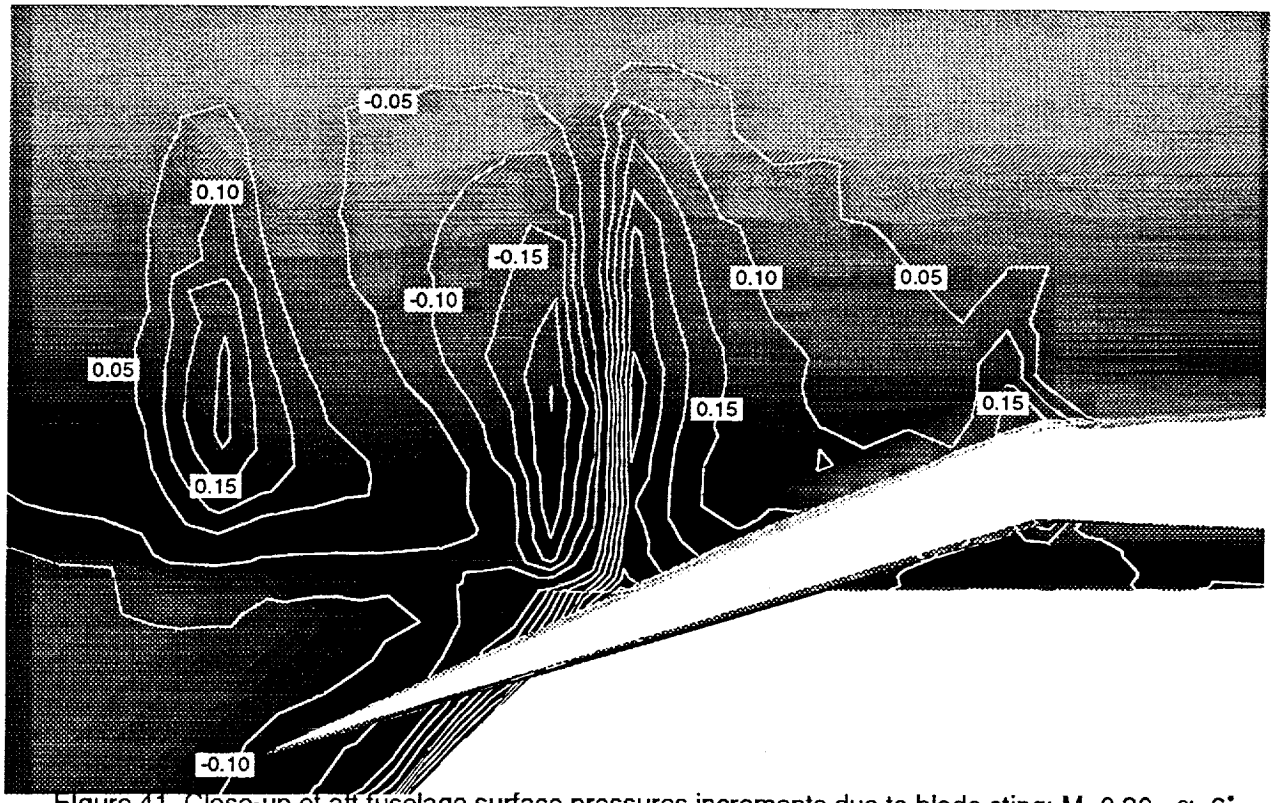

Figure 41. Close-up of aft fuselage surface pressures increments due to blade sting; M=0.30, α=6°, δ_{HT}=0°, δ_{LE}=30°/30°, δ_{TE}=20°/20°, (ΔC_p=0.05).

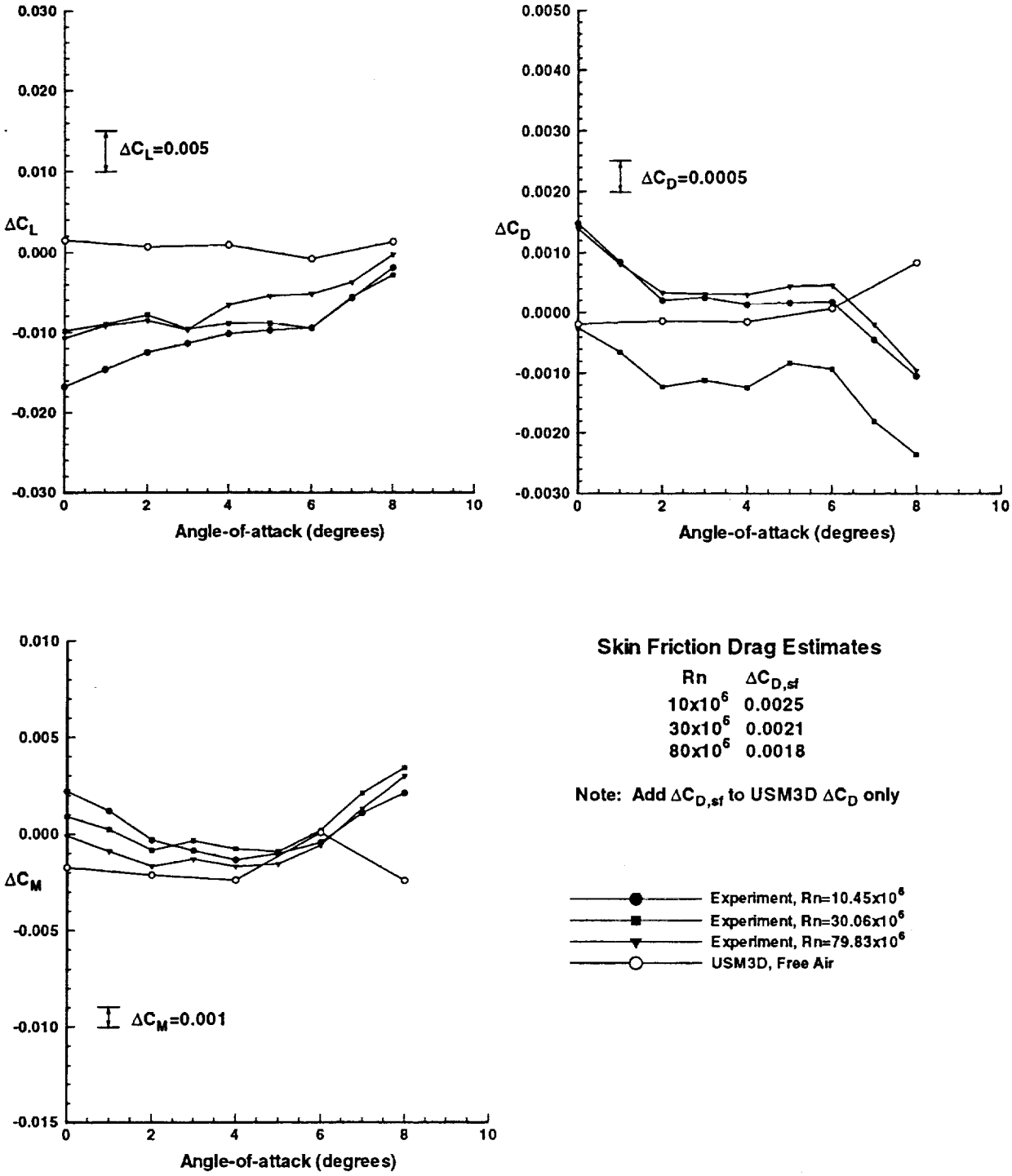

Figure 42. Afterbody / tail surface force and moment increments corrected for predicted blade sting interference; M=0.95, δ_{HT}=0°, δ_{LE}=0°/10°, δ_{TE}=0°/3°

Table 1: HSR Reference H Grids Developed

$\delta_{LE(IB)}$/ $\delta_{LE(OB)}$	$\delta_{TE(IB)}$/ $\delta_{TE(OB)}$	δ_{HT}	Sting	Number of nodes	Number of cells
30°/30°	20°/20°	0°	No Sting	223,278	1,221,259
30°/30°	20°/20°	0°	Blade Sting	223,380	1,216,331
0°/10°	0°/3°	0°	No Sting	115,306	839,865
0°/10°	0°/3°	0°	Blade Sting	200,007	1,082,028
0°/10°	0°/3°	0°	Circular Aft Body/Sting	172,244	929,761
0°/10°	0°/3°	-5°	No Sting	147,623	797,631
0°/10°	0°/3°	-5°	Blade Sting	197,576	1,068,858
0°/0°	0°/0°	0°	No Sting	95,687	505,634
0°/0°	0°/0°	0°	Blade Sting	111,899	591,857

Table 2: HSR Reference H Configurations Analyzed

$\delta_{LE(IB)}$/ $\delta_{LE(OB)}$	$\delta_{TE(IB)}$/ $\delta_{TE(OB)}$	δ_{HT}	Sting	Mach Number	Angle-of-attack
30°/30°	20°/20°	0°	No Sting	0.30	6°
30°/30°	20°/20°	0°	Blade Sting	0.30	6°
0°/10°	0°/3°	0°	No Sting	0.95	0°,2°,4°,6°,8°
0°/10°	0°/3°	0°	Blade Sting	0.95	0°,2°,4°,6°,8°
0°/10°	0°/3°	0°	Circular Aft Body/Sting	0.95	0°,4°
0°/10°	0°/3°	-5°	No Sting	0.95	2°,4°,6°
0°/10°	0°/3°	-5°	Blade Sting	0.95	2°,4°,6°
0°/0°	0°/0°	0°	No Sting	2.4	4°
0°/0°	0°/0°	0°	Blade Sting	2.4	4°

Table 3: Blade Sting Interference Effects, M=0.95, δ_{LE}=0°/10°, δ_{TE}=0°/3°.

Angle-of-attack	δ_{HT}	ΔC_L	ΔC_D	ΔC_M
0°	0°	0.0428	-0.0015	-0.00959
2°	0°	0.0361	0.00065	-0.00662
4°	0°	0.0333	0.0014	-0.00558
6°	0°	0.0318	0.0020	-0.00601
8°	0°	0.0236	0.0041	-0.00801
2°	-5°	0.0350	0.00058	-0.00577
4°	-5°	0.0318	0.00166	-0.00433
6°	-5°	0.0314	0.00284	-0.00379

REPORT DOCUMENTATION PAGE

Form Approved
OMB No. 0704-0188

1. AGENCY USE ONLY *(Leave blank)*	2. REPORT DATE	3. REPORT TYPE AND DATES COVERED
	December 1999	Contractor Report

4. TITLE AND SUBTITLE
Computational Assessment of Aft-Body Closure for the HSR Reference H Configuration

5. FUNDING NUMBERS
C NAS1-19672
WU 537-07-20-03

6. AUTHOR(S)
W. Kelly Londenberg

7. PERFORMING ORGANIZATION NAME(S) AND ADDRESS(ES)
ViGYAN, Inc.
30 Research Drive
Hampton, VA 23666

8. PERFORMING ORGANIZATION REPORT NUMBER

9. SPONSORING/MONITORING AGENCY NAME(S) AND ADDRESS(ES)
National Aeronautics and Space Administration
Langley Research Center
Hampton, VA 23681-2199

10. SPONSORING/MONITORING AGENCY REPORT NUMBER
NASA/CR-1999-209521

11. SUPPLEMENTARY NOTES
Langley Technical Monitor: Neal T. Fink

12a. DISTRIBUTION/AVAILABILITY STATEMENT
Unclassified–Unlimited
Subject Category 02 Distribution: Nonstandard
Availability: NASA CASI (301) 621-0390

12b. DISTRIBUTION CODE

13. ABSTRACT *(Maximum 200 words)*

A study has been conducted to determine how well the USM3D unstructured Euler solver can be utilized to predict the flow over the High Speed Research Reference H configuration with an ultimate goal of prediction of sting interference so after body closure effects may be evaluated. This study has shown that the code can be used to predict the interference effects of a lower mounted blade sting with a high degree of confidence. It has been shown that wing and fuselage pressures, both levels and trends, can be predicted well. Force and moment levels are not predicted well but experimental trends are predicted. Based upon this, predicted force and moment increments are assumed to be predicted accurately. Deflection of the horizontal tail was found to cause a non-linear increment from the non-deflected sting interference effects.

14. SUBJECT TERMS	15. NUMBER OF PAGES
Unstructured grids; High-speed research; Aft-body closure; Euler	42
	16. PRICE CODE: A03

17. SECURITY CLASSIFICATION OF REPORT	18. SECURITY CLASSIFICATION OF THIS PAGE	19. SECURITY CLASSIFICATION OF ABSTRACT	20. LIMITATION OF ABSTRACT
Unclassified	Unclassified	Unclassified	UL